



Anisotropic viscoplasticity explains slow-slip M_0 - T scaling at convergent plate margins

An Yin*, Zhoumin Xie

Department of Earth, Planetary, and Space Sciences, University of California, Los Angeles, CA 90095-1567, USA



ARTICLE INFO

Keywords:
Slow earthquakes
Viscoplasticity
Energy balance
Scaling between seismic moments and event durations

ABSTRACT

In this study, we quantify the mechanisms that govern two related observations with regard to deep (15–50 km) subduction-zone aseismic slow-slip events (SSEs): (i) the linear scaling relationship between seismic moments (M_0) and event durations (T), and (ii) the direction-dependent slow-slip rupture speeds. Geological observations suggest that deep-subduction slow-slip shear zones are anisotropic and viscoplastic; the anisotropy is due to the presence of dip-parallel mafic lineaments created by seamount subduction, whereas the viscoplasticity is due to deformation of mixed brittle mafic and ductile felsic materials. We postulate that a dip-parallel (= slip direction) mafic lineament in an overall felsic slow-slip shear zone acts as a stress guide, which localizes initial slow-slip rupture in the dip direction. Subsequent stress concentration along the dip-parallel edges of the early ruptured lineament leads to along-strike rupture, with the rupture front propagating through the felsic shear zone. The second-phase slip-area expansion maintains a constant dip-parallel rupture-zone length, inherited from the length of the early ruptured mafic lineament. By combining an energy balance equation with a two-phase rupture model outlined above, we obtain the first analytical expression of the observed linear scaling law in the

form of $M_0 = c_0 T$, where $c_0 = \frac{4\gamma_1 \Delta z G^2 L^2 \left[\frac{(\bar{\mu}_s - \bar{\mu}_d) g H \Delta z}{\eta_e \cos(\delta)} + V_{FW} \right]}{[2L \Delta z (\bar{\mu}_s^2 - \bar{\mu}_d^2) (\rho g H)^2 - 4\gamma_1 G (L + \Delta z) - \rho \Delta z L G (V_{FW} + v_d)^2]}$; the observed value of this empirical

constant is between $10^{11.5}$ and $10^{13.5}$ J/s. In the above expression, L , H , Δz , δ , G , η_e , $\bar{\mu}_s$, and $\bar{\mu}_d$ are length, depth, thickness, dip angle, shear rigidity, effective viscosity, and effective coefficients of static and dynamic friction of the slow-slip shear zone, γ_1 is surface-energy density of the initially ruptured mafic lineament, ρ is overriding-plate density, V_{FW} and v_d are subducting-plate and slow-slip velocities, and g is surface gravity. Our model, based on the assumed shear-zone anisotropy, successfully predicts fast (~ 100 km/h) dip-parallel rupture along high-viscosity ($\sim 10^{20}$ Pa s) mafic lineaments and slow (2–10 km/day) strike-parallel rupture through low-viscosity ($\sim 10^{17}$ Pa s) felsic materials during a deep-subduction slow-slip event.

1. Introduction

Slow earthquakes are dominated by those occurring downdip of seismogenic megathrusts along seismic-aseismic transition zones at plate convergent margins (Fig. 1a) (Schwartz and Rokosky, 2007; Peng and Gomberg, 2010; Beroza and Ide, 2011; Wallace et al., 2016; Araki et al., 2017; Gao and Wang, 2017). Slow earthquakes are slow fault-slip processes with slip rates 2–3 orders of magnitude slower than those of regular earthquakes (e.g., Bürgmann, 2018). The slow-slip phenomena along subduction zones are variably expressed as aseismic slow-slip events (SSEs) (Dragert et al., 2001; Hirose and Obara, 2005; Bartlow et al., 2011; Wallace et al., 2012; Li et al., 2016; Rousset et al., 2017), episodic tremor and slip (ETS) events (Rogers and Dragert, 2003; Obara et al., 2004; Obara and Kato, 2016; Wang and Tréhu, 2016), primary

and secondary propagation of slow-slip fronts (e.g., Ghosh et al., 2010; Houston et al., 2011; Peng and Rubin, 2016; Hawthorne et al., 2016; Blettery et al., 2017), and tectonic tremors resulting from clustered low (1–5 Hz) to very low (0.01–0.05 Hz) frequency earthquakes (LFEs and VLFs) (e.g., Obara, 2002; Ito et al., 2007; Shelly et al., 2007; Ide et al., 2008; Bostock et al., 2015, 2017; Obara and Kato, 2016). Ide et al. (2007) first recognized the slow fault-slip phenomena to follow a linear scaling law between seismic moments (M_0) and event durations (T). The law, commonly expressed as $M_0 = c_0 T$, has an empirical constant of $c_0 = \sim 10^{12.5 \pm 1.0} \text{ N m s}^{-1}$ (or in J/s) (Fig. 1b). This linear scaling differs from the well known $M_0 \sim T^3$ scaling for regular earthquakes, with the latter implying a self-similar source process (Aki, 1967; Houston, 2001; Denolle and Shearer, 2016).

Despite a shared scaling relationship and despite occurring along

* Corresponding author.

E-mail address: ayin54@gmail.com (A. Yin).

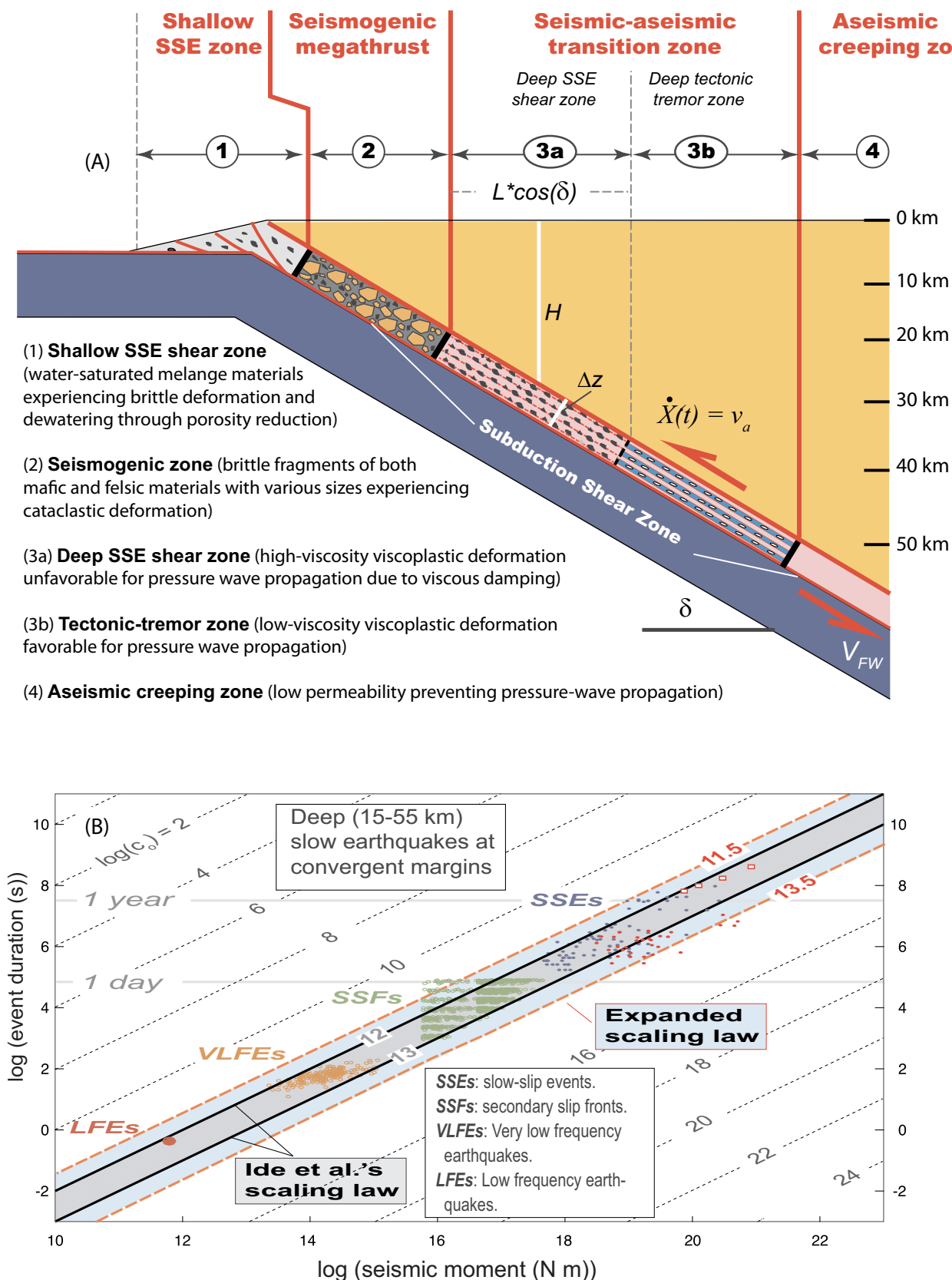


Fig. 1. (A) Division of an idealized subduction zone that consists of four segments as labelled. The seismic-aseismic transition zone, which is the focus of this study, may split into an updip slow-slip shear zone and a downdip tectonic-tremor shear zone. Also shown are key geometric and kinematic parameters used in this study. (B) An updated moment–duration scaling law of Ide et al. (2007) based on data pertinent to deep (15–50 km) subduction-zone slow earthquakes. The data include aseismic slow-slip events and seismic tectonic tremors, with sources from Bletery et al. (2017), Li et al. (2016) and Rousset et al. (2017). The diagonally dotted lines show $\log(c_0)$ values after Bletery et al. (2017), where c_0 represents the moment-releasing rate. Note that the data obtained from Rousset et al. (2017) display a systematic shift to the right of the plot when compared to SSE data from the same area obtained by other researchers using different methods (e.g., Radiguet et al., 2012, 2016). (For interpretation of the references to colour in this figure legend, the reader is referred to the web version of this article.)

the same subduction zone, deep-subduction slow fault-slip phenomena may have different spatial distributions and different mechanical origins. For example, SSEs occur aseismically and rupture either updip or across the related tectonic-tremor zone (e.g., Dragert and Wang, 2011; Bartlow et al., 2011; Ochi and Kato, 2013; Hall et al., 2018; Michel et al., 2018). Specifically, long-term (months to years) SSEs are located mostly updip of the related tectonic-tremor zone as shown in Fig. 1a, whereas short-term (days to weeks) SSEs generally overlap the related tectonic-tremor zone (e.g., Bartlow et al., 2014; Obara and Kato, 2016; Hall et al., 2018). The close spatiotemporal relationship between short-term SSEs and tectonic tremors (e.g., Bartlow et al., 2011; Dragert and Wang, 2011; Ochi and Kato, 2013; Obara and Kato, 2016; Hall et al., 2018; Michel et al., 2018) leads to the findings that (1) slow-slip rupture is 2–3 orders faster in the dip (=slip) direction (~ 100 km/h) than in the strike direction (5–10 km/day) of the shear zone, and (2) along-strike rupture maintains a constant downdip length (Shelly et al., 2007; Ghosh et al., 2010; Michel et al., 2018).

In this study, we focus on two issues related to *aseismic slow-slip events* along deep (15–50 km) subduction zones: (i) the mechanical origin of their linear scaling relationship (Fig. 1b), and (ii) the mechanism that controls the direction-dependent slow rupture speeds. Although these two issues are related, current research has not integrated them into a unified mechanical model. For example, the fault-interaction model of Romanet et al. (2018) is capable of generating the linear scaling law but does not predict the anisotropic rupture process, whereas the heterogeneous-fault model of Ando et al. (2010) explains direction-dependent rupture speeds but the model itself requires the assumption that slow-slip rupture obeys the observed linear scaling law.

Early researchers (e.g., Cloos, 1992; Bebout and Barton, 2002; Ando et al., 2010; Rubin, 2011) suggest that anisotropy may have played an important role in the deformation processes during plate subduction (also see Simons et al., 2011; Duan, 2012; Yang et al., 2012, 2013; Wang and Bilek, 2014; Yin, 2018; Todd et al., 2018). At a convergent margin, the first-order subduction-zone anisotropy may be defined by slip-parallel (=dip direction in this study) lineaments composed dominantly of high-viscosity and high-permeability mafic materials derived from seamount subduction (e.g., Cloos, 1992). Such lineaments may be spaced widely, > 100 s km apart as indicated by the modern seafloor topography (Cloos, 1992) (also see Fig. 2a). These mafic lineaments are embedded in an overall felsic shear zone with the materials dominantly derived from the nearby arc and continent. Inferences from seafloor topography indicate that the seamount-induced mafic lineaments in a subduction shear zone could have a strike-parallel dimension of 10 s km (Cloos, 1992). However, mafic and ultramafic bodies of this size are rarely seen in the exhumed subduction zones; they are typically in the range of less than a few km and the size reduction has been attributed to distension of the subducted seamounts (e.g., Festa et al., 2010). At a finer scale, deep subduction shear zones may consist of slip-parallel (=dip-parallel) mineral stretching lineations at a few mm scale and mafic-ultramafic lineaments created by shear-zone deformation, ranging in size from a few m to 100 s m (Bebout and Barton, 2002; Grove et al., 2008; Behr et al., 2018) (Fig. 3).

The above observations allow us to relate fast along-dip and slow along-strike rupture of a slow-slip event to shear-zone anisotropy. Specifically, initial rupture is likely to follow a high-viscosity dip-parallel mafic lineament. Such a scenario has been suggested by Cloos (1992) for the genesis of megathrust subduction-zone earthquakes, and appears to be confirmed by direct and inferred seismological observations (e.g., Simons et al., 2011; Duan, 2012; but see Wang and Bilek, 2014). Expanding on this concept, we suggest that the presence of a strong mafic lineament in an overall felsic slow-slip shear zone controls a two-phase rupture kinematics; each is unidirectional with a fixed

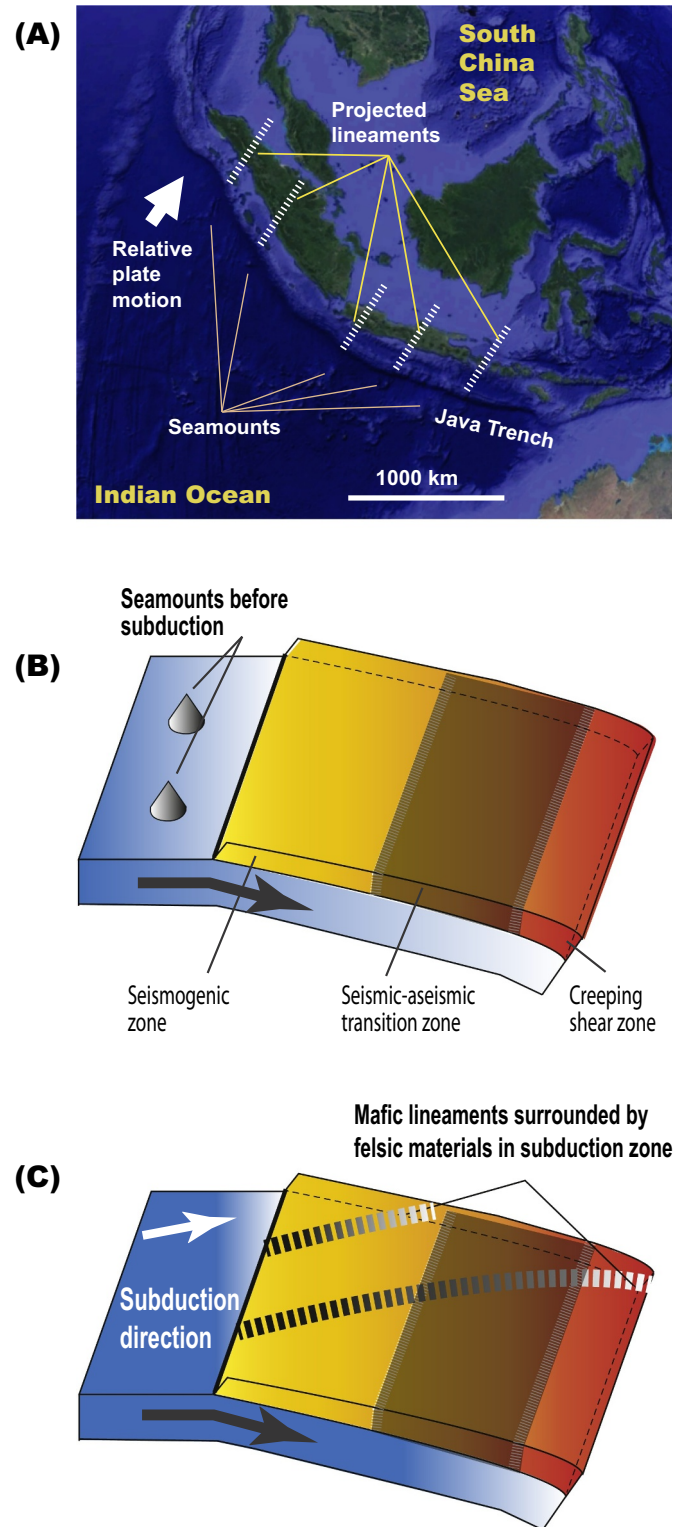


Fig. 2. (A) Seamounts as point sources of mafic-rich high-viscosity and high-porosity linear streaks in a subduction shear zone with an example from the Java subduction system along the northern rim of Indian Ocean. (B) and (C) show the positions of seamounts before subduction and their linear tracks in the subduction zone during subduction. The streaks are parallel to the plate convergence direction, which is assumed to be the same as the dip direction in this study.

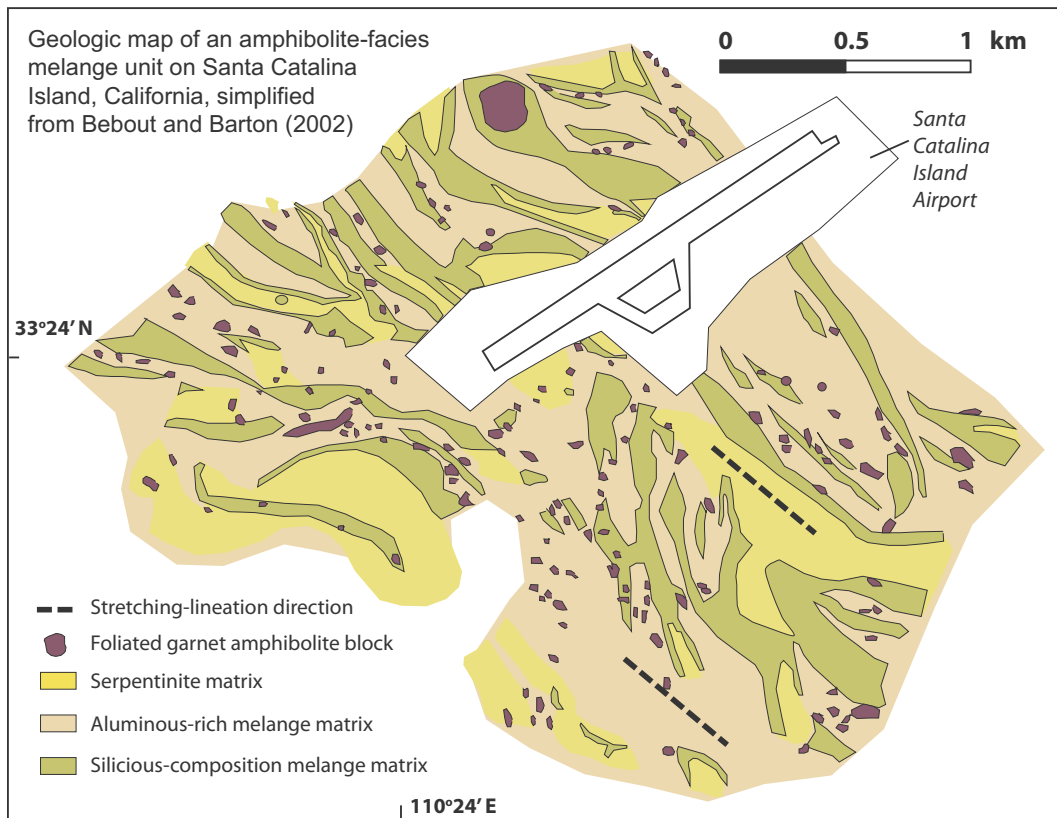


Fig. 3. Linear streaks of discontinuous bodies of mafic and ultramafic rocks in an amphibolite-facies Mesozoic subduction shear zone on the Santa Catalina Island, southern California (simplified from [Bebout and Barton, 2002](#)).

width of the rupture zone. First, the strong mafic lineament localizes along-dip rupture at the onset of a slow-slip event ([Fig. 4a](#)). The rupture front is a straight line parallel to the shear-zone strike, whereas the corresponding rupture direction is parallel to the shear-zone dip (=slip) direction ([Fig. 4a](#)). Once created, the dip-parallel edges of the early ruptured strip become crack tips where stress concentrates and strain accumulates against the nearby felsic shear-zone materials ([Fig. 4b](#)). The concentration of the stress causes the second-phase expansion of the slip zone in the strike direction through progressive shear failure of the rupture-zone edges. During the second-phase slow-slip rupture, the rupture front is also assumed to be a straight line parallel to the shear-zone dip direction, and the corresponding rupture is in the strike direction perpendicular to the slip direction ([Figs. 4b and c](#)). The dip-parallel length of the rupture zone in the second rupture phase is constant, interpreted to have inherited from the length of the initially ruptured mafic lineament. In this study, we combine the proposed two-stage rupture model shown in [Fig. 4](#) with an energy balance equation to derive the first analytical expression of the linear scaling law of [Ide et al. \(2007\)](#). This result allows us to relate [Ide et al.'s \(2007\)](#) scaling constant to a suite of geometric and mechanical properties of a convergent margin that generates deep subduction slow-slip events.

2. Viscoplastic quenching mechanism

A central debate in the studies of slow earthquakes is the essential physics of quenching mechanisms that prevent a slow-slip event to grow into a runaway fast earthquake ([Liu and Rice, 2007](#); [Rubin, 2008](#); [Segall et al., 2010](#); [Bürgmann, 2018](#)). The proposed quenching mechanisms include (1) rate-state friction under a fine-tuned critically stable condition ([Liu and Rice, 2007](#)), (2) high-velocity strengthening (e.g., [Shibazaki and Shimamoto, 2007](#); [Hawthorne and Rubin, 2013](#); [Shimamoto and Noda, 2014](#)), (3) slip-induced dilation ([Rubin, 2008](#);

[Segall et al., 2010](#)), (4) heterogenous faults with variable frictional properties ([Ando et al., 2010](#); [Luo and Ampuero, 2018](#)), and (5) viscoplastic retardation (e.g., [Hayman and Lavier, 2014](#); [Fagereng et al., 2014](#); [Fagereng and den Hartog, 2017](#); [Yin et al., 2018](#); [Behr et al., 2018](#); [Platt et al., 2018](#)). The first four mechanisms are based on rate-state friction laws, whereas the last is based on experimental results relevant to deep subduction slow-slip deformation (e.g., [Chester, 1995](#); [Pec et al., 2016](#)) and field observations of exhumed deep subduction shear zones (e.g., [Hayman and Lavier, 2014](#); [Behr et al., 2018](#)). Below, we only focus on the viscoplastic quenching mechanism of [Yin et al. \(2018\)](#) as it provides the constitutive equations that lead to our analytical expression of the empirical scaling law of [Ide et al. \(2007\)](#).

We assume slip weakening at the onset of slow-slip deformation but neglect the details of weakening paths, such as those governed by rate-state friction laws; the shear stress (τ_{vp}) relates to the shear-strain rate ($\dot{\epsilon}_{vp}$) in a viscoplastic slow-slip shear zone by:

$$\dot{\epsilon}_{vp} = \frac{[V_{FW} + \dot{X}(t)] \cos(\delta)}{\Delta z} = \frac{(\tau_{vp} - Y_d)}{\eta_e} \text{ if } |\tau_{vp}| \geq Y_s \quad (1a)$$

$$\dot{\epsilon}_{vp} = \frac{[V_{FW} + \dot{X}(t)] \cos(\delta)}{\Delta z} = 0 \text{ if } |\tau_{vp}| < Y_s \quad (1b)$$

where

$$Y_s = \rho g H \bar{\mu}_s$$

$$Y_d = \rho g H \bar{\mu}_d$$

are static and dynamic yield strengths, with static strength Y_s greater than the dynamic strength Y_d . Other parameters in the above equations are defined as follows (also see [Table 1](#) and [Fig. 1a](#)): Δz is shear-zone thickness, η_e is shear-zone effective viscosity, δ is shear-zone dip angle, H is average shear-zone depth, $\bar{\mu}_s$ is effective coefficient of static friction, $\bar{\mu}_d$ is effective coefficient of dynamic friction, V_{FW} is subducting-

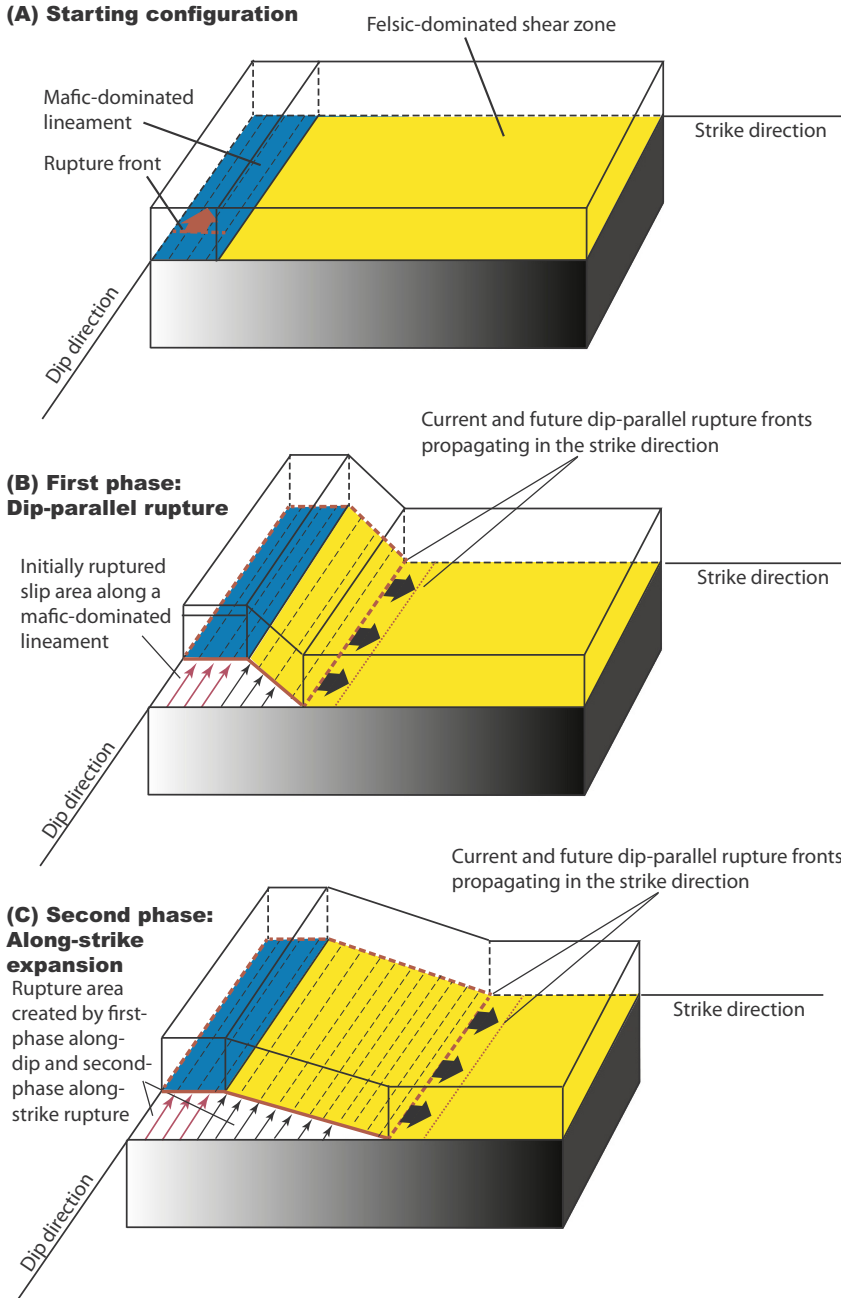


Fig. 4. A two-phase slow-slip rupture model during a slow-slip event. (A) A slow-slip shear zone consists of a high-viscosity mafic lineament (shown as a narrow strip of a blue surface) in an overall low-viscosity felsic shear zone (shown as a yellow surface) before the onset of a slow-slip event. (B) The first-phase along-dip slow-slip rupture propagates along a strong mafic lineament at the onset of a slow-slip event. (C) The second-phase slip-zone expansion has the rupture front propagating in the strike direction. The along-strike rupture is assumed to occur with a constant dip-parallel rupture-zone length and a constant shear-zone thickness (not shown here). (For interpretation of the references to colour in this figure legend, the reader is referred to the web version of this article.)

plate (i.e., footwall) velocity, and $\dot{X}(t)$ is overriding-plate (i.e., hanging-wall) velocity. The above constitutive equations assume an instantaneous drop in shear-zone plastic strength at the onset of a slow-slip event, which requires

$$\tau_{vp}(t = 0) = Y_s = \rho g H \bar{\mu}_s$$

$$\tau_{vp}(t \geq 0) = Y_d = \rho g H \bar{\mu}_d$$

Using Eq. (1b), we obtain $\dot{X}(t = 0) = V_{cr}$, which is defined by

$$V_{cr} = \frac{(\bar{\mu}_s - \bar{\mu}_d) \rho g H \Delta z}{\eta_e \cos(\delta)} - V_{FW} \quad (2)$$

Here, V_{cr} represents the upper limit of the hanging-wall velocity at the onset of a slow-slip event. The above relationship quantifies the quenching mechanism, which indicates that the slip velocity along the viscoplastic shear zone is retarded by shear-zone viscosity η_e . Specifically, $V_{cr} = V_{FW}$ when $\eta_e \rightarrow \infty$, which means that the shear zone would

be permanently locked. Eq. (2) also indicates that V_{cr} increases with differential friction ($\bar{\mu}_s - \bar{\mu}_d$). As shown in Yin et al. (2018), $\dot{X}(t) \approx V_{cr}$ and is nearly constant (i.e., not time-dependent) when $\eta_e \geq 10^{16}$ Pa under deep-subduction slow-slip conditions. Based on this result, we assume in this study that $v_a \approx V_{cr}$, where v_a is the average slow-slip velocity parallel to the shear zone (Fig. 1a). The stress drop magnitudes between 1 kPa and 100 kPa associated with deep subduction slow-slip events (e.g., Bletery et al., 2017) require $(\bar{\mu}_s - \bar{\mu}_d)$ to be 10^{-4} to 10^{-6} (Yin et al., 2018). For a shear-zone viscosity of 10^{17} Pa s, this yields a critical velocity of 10^{-7} to 10^{-8} m s $^{-1}$, similar in magnitudes to those observed from geodetic measurements (e.g., Dragert et al., 2001). The ‘‘critical velocity’’ concept provides a physical basis for slow-earthquake mechanical models that assume an upper cutoff velocity for low-velocity weakening when applying rate-state friction laws (e.g., Colella et al., 2011, 2013; Shibazaki et al., 2012; Shibazaki and Shimamoto, 2007; Hawthorne and Rubin, 2013; Shimamoto and Noda, 2014). The low estimated critical velocity values of 10^{-7} to 10^{-8} m s $^{-1}$ also

Table 1
Model parameters.

$A(t)$, rupture-area evolution during a slow-slip event
$c_0 = 10^{11.5}$ to $10^{13.5}$ N m s ⁻¹ , empirical constant in Ide et al.'s (2007) scaling law with updated data shown in Fig. 1b
$g = 10$ m s ⁻² , gravitational acceleration
$G = 30$ GPa, shear rigidity
$H = 35$ km, average depth to the slow-slip shear zone
$L = 65$ km, down-dip length of the slow-slip shear zone
M_0 and T , seismic moment and event duration
$N[x(t)]$, along-strike distribution-density function of dip-parallel mafic lineaments
$V_{cr} = 10^{-8}$ m s ⁻¹ , critical velocity for initiating viscoplastic slow-slip deformation
$V_{FW} = 10^{-11}$ m s ⁻¹ , subducting-plate (footwall) velocity parallel to shear zone
v_a , average overriding-plate (hanging wall) velocity parallel to shear zone during a slow-slip event
W_0 , slip-zone width generated by first-phase along-dip rupture following a dip-parallel lineament
$W_m(t)$, slip-zone width generated by second-phase along-strike rupture of felsic shear-zone materials
$W_d(t)$, slip-zone width generated by second-phase along-strike rupture of mafic lineaments
$W_s(t) = W_d(t) + W_m(t)$, total slip-zone width generated by second-phase along-strike rupture
$W_e(t) = W_0 + W_s(t)$, effective slip-zone width
$X(t)$, hanging-wall slip history (not used in the model)
Y_s , static plastic yield strength
Y_d , dynamic plastic yield strength
$\Delta z = 4$ km, shear-zone thickness
$\delta = 0^\circ$, shear-zone dip angle
$\bar{\mu}_s$, effective coefficient of static friction
$\bar{\mu}_d = 0.01$, effective coefficient of dynamic friction
$\Delta\bar{\mu} = (\bar{\mu}_s - \bar{\mu}_d) = 10^{-6}$ to 10^{-4} , differential coefficient of effective friction
η_e , effective viscosity of the shear zone
$\eta_{e(d)}$, effective viscosity of dip-parallel lineament along which first-phase rupture occurs
γ_1 , surface-energy density of the initially ruptured dip-parallel mafic lineament
γ_{1-a} , surface-energy density of an instantaneously ruptured segment of a dip-parallel lineament
γ_{1-b} , surface-energy density of time-dependent ruptured region along a dip-parallel lineament
γ_2 , surface-energy density of the felsic materials in the slow-slip shear zone
$\rho = 3000$ kg m ⁻³ , overriding-plate density
$\Delta\tau = 10$ – 100 kPa, stress drop during a slow-slip event
ϵ_0 , scaling constant between rupture speed and rupture time

explain a lack of detectable seismic waves from slow-slip deformation along deep (15–50 km) subduction slow-slip shear zones, as radiation of seismic energy critically depends on the magnitudes and spatial gradients of slip and rupture velocities (e.g., Madariaga, 1977; Ohnaka and Yamashita, 1989).

3. Anisotropic rupture

3.1. Kinematic model of two-phase rupture

Based on the two-stage rupture model shown in Fig. 4 and noting that tremor migration is 2–3 orders of magnitude faster in the dip direction than that in the strike direction of a subduction zone (Shelly et al., 2007; Ghosh et al., 2010), we treat (but see a finite-rupture speed case discussed later in the paper) the dip-parallel rupture zone to have been created instantaneously with an area of $A_0 = W_0L$ (Fig. 5). Here, W_0 is along-strike width and L is dip-parallel length of the initially ruptured strip along a linear stress guide (i.e., a high-viscosity mafic lineament). The subsequent along-strike rupture has a time-dependent area $A_s(t)$, which is defined by $A_s(t) = LW_s(t)$ assuming that L is constant during lateral rupture and $W_s(t)$ evolves with time (Fig. 5). We now define the effective (i.e., total) rupture-zone width $W_e(t)$ as the sum resulting from both dip-parallel and strike-parallel rupture expressed as

$$W_e(t) = W_0 + W_s(t)$$

The second-phase along-strike expansion of the slip zone may involve additional dip-parallel lineaments. The total slip-zone width of

the second-phase along-strike rupture under this condition can be written as

$$W_s(t) = W_d(t) + W_m(t)$$

where $W_d(t)$ is the total width of the dip-parallel mafic lineaments encountered during the along-strike rupture at time t , and $W_m(t)$ is the total width of the ruptured weak felsic shear zone at time t (Fig. 5). Insert this relationship into the equation of $W_e(t) = W_0 + W_s(t)$, we get

$$W_e(t) = W_0 + W_m(t) + W_d(t) \quad (3)$$

where $W_d(t) = \sum_1^{n(t)} W_{d(i)}$ and $W_m(t) = \sum_1^{n(t)} W_{m(i)}$. Here, $n(t)$ varying with time is the number of mafic lineations in the shear zone that were swept by the second-phase rupture at time t (Fig. 5). Assume that dip-parallel lineaments encountered by the second-phase along-strike rupture follows the distribution of

$$N[x(t)] = N[t] = \frac{W_d(t)}{W_m(t) + W_d(t)} \quad (4a)$$

where $x(t)$ represents the distance of rupture-front migration since the onset of the second-phase rupture (i.e., $x(t) = W_s(t) = W_m(t) + W_d(t)$). The above equation can be rewritten as

$$W_d(t) = \frac{N(t)}{1 - N(t)} W_m(t) \quad (4b)$$

A special case of the above equation is $N(t) = N_0$, where N_0 is a constant. In this case, we have.

$$W_e(t) = \frac{1}{1 - N_0} W_m(t) + W_0 \quad \text{for } N_0 > 0 \quad (5a)$$

$$W_e(t) = W_m(t) + W_0 \quad \text{for } N_0 = 0 \quad (5b)$$

When spacing $S_{d(i)}$ and individual width $W_{d(i)}$ are constant, N_0 becomes

$$N_0 = \frac{W_{d(i)}}{S_{d(i)}}$$

Eq. (5b) represents a situation when the first-phase rupture in the dip direction (Figs. 4 and 5) involves a single dip-parallel lineament at the initial stage, while the second-phase rupture in the strike direction does not encounter any dip-parallel lineaments when moving through the felsic shear zone. This is a key condition, as shown below, that leads to an analytical expression of the empirically observed linear scaling law for deep subduction slow-slip events.

A more complicated case is when $N(t)$ is not constant, and its temporal evolution depends on $W_m(t)$ and $W_d(t)$. As shown below, a 1-D rupture speed in a homogeneous and isotropic viscoplastic shear zone has the following relationship:

$$W_d(t) = \epsilon_0(\eta_e)t^2 \quad (5c)$$

where ϵ_0 is a proportional constant when the shear-zone viscosity η_e is fixed. This particular condition, when applied to the rupture duration of individual lineaments, leads to a cubic scaling law for deep subduction slow-slip events as we show below.

3.2. Mechanics of instantaneous along-dip rupture

We consider the initial dip-parallel rupture along a mafic lineament as an instantaneous event. A more general case with a finite along-dip rupture speed is discussed later in the paper. Under this assumption and using an energy balance equation that neglects the effect of seismic radiation, we can relate the width of the initially ruptured linear strip W_0 to the geometric, kinematic, and mechanical properties of a slow-slip shear zone by the following relationship (see Appendix for details):

$$W_0 = \frac{2\gamma_1 L \Delta z}{\left[\frac{L \Delta z}{2G_1} (\bar{\mu}_{s1}^2 - \bar{\mu}_{d1}^2) (\rho g H)^2 - 2\gamma_1 (L + \Delta z) - \frac{\rho \Delta z L}{2} [V_{FW} + v_a]^2 \right]} \quad (6)$$

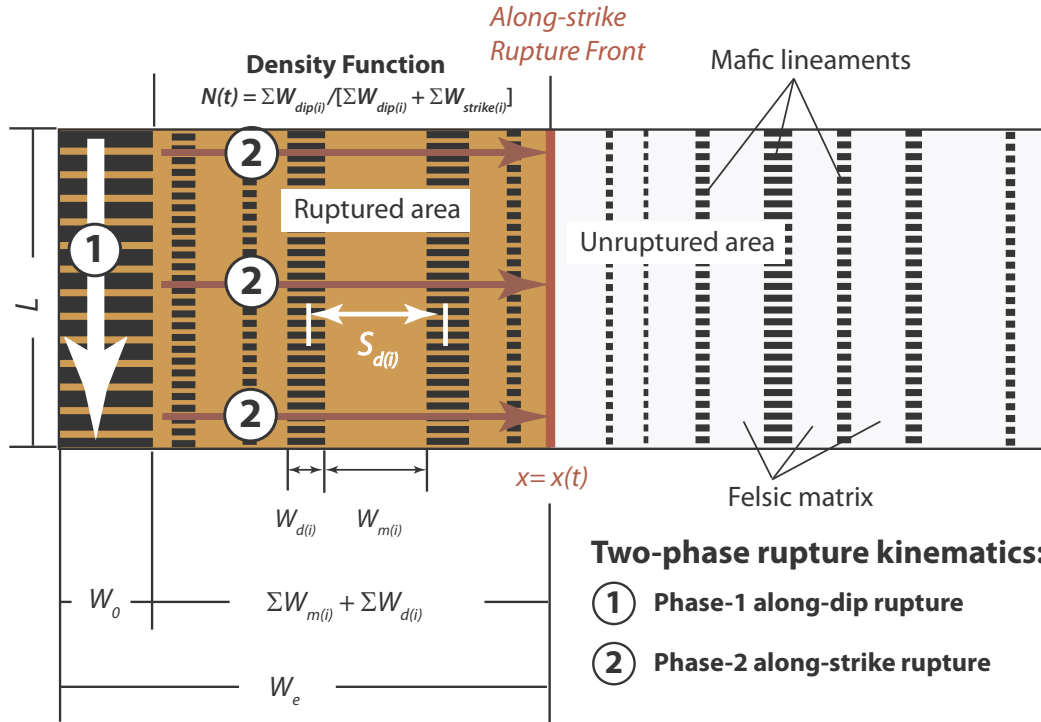


Fig. 5. A hypothetical slow-slip shear-zone plane illustrating the key geometric parameters discussed in the text. The shear zone consists of dip-parallel higher-viscosity mafic lineaments (thick dashed lines) surrounded by low-viscosity felsic shear-zone materials. The rupture process during a slow-slip event occurs in two phases: the first phase by along-dip rupture following a strong mafic lineament, whereas the second phase by lateral expansion of the early ruptured strip in the strike direction. An end-member case is that the first-phase rupture involves a single mafic lineament while the second-phase rupture involves only the felsic shear-zone materials. As shown in the text, this particular condition leads to a linear scaling relationship between seismic moments and event durations.

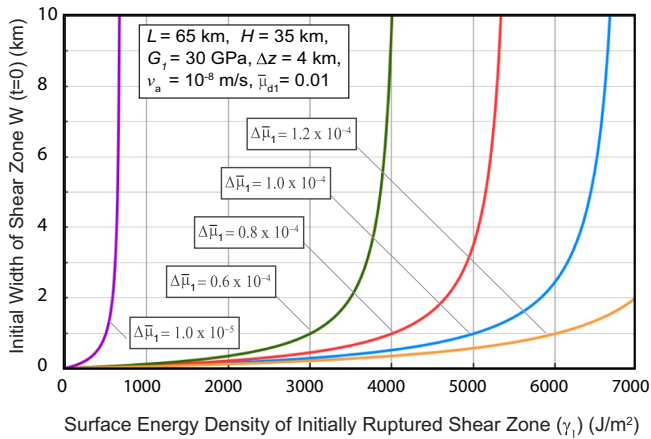


Fig. 6. Initial slip-zone width as a function of surface-energy density with variable differential friction coefficients.

where γ_1 , G_1 , $\bar{\mu}_{s1}$, and $\bar{\mu}_{d1}$ are surface-energy density (J m^{-2}), shear rigidity, effective coefficient of static friction, and effective coefficient of dynamic friction of the dip-parallel high-viscosity mafic lineament along which initial first-phase rupture occurs. Fig. 6 shows how the initial width W_0 varies with surface-energy density γ_1 . In this plot, we vary $\Delta\bar{\mu}_1 = (\bar{\mu}_{s1} - \bar{\mu}_{d1})$ and assume $V_{FW} = 10^{-11} \text{ m s}^{-1}$ and $v_a = 10^{-8} \text{ m s}^{-1}$. We also set $\bar{\mu}_{d1} = 0.01$ that represents a nearly lithostatic pore-fluid-pressure condition based on the work of Behr et al. (2018) and Audet and Schaeffer (2018) that is relevant to deep subduction slow-slip events (Table 1). The values of $\Delta\bar{\mu}_1$ are estimated to be 10^{-6} to 10^{-4} from stress drops of 1–100 kPa associated with deep subduction low-frequency to very low-frequency earthquakes (e.g., Ide et al., 2007; Bletery et al., 2017). For $\Delta\bar{\mu}_1 = 10^{-4}$ and $W_0 = 10 \text{ km}$

estimated from the results of Ghosh et al. (2010), we find $\gamma_1 = \sim 6500 \text{ J/m}^2$ (Fig. 6). This value is remarkably similar to those estimated based on experimental and seismological observations for a fault slip of $\sim 0.01 \text{ m}$ (see Fig. 6 of Nielsen et al., 2016).

3.3. Mechanics of along-strike rupture and \dot{M}_0 scaling

We now examine the controlling factors for the second-phase along-strike rupture during a slow-slip event. Based on an energy balance equation that neglects the effect of seismic radiation, the time-dependent rupture history can be quantified by the evolving slip-zone width expressed as (see Appendix for detailed derivation):

$$\dot{W}_m(t) + \frac{B_W}{A_W + B_W t} W_m(t) = 0 \quad (7)$$

where

$$A_W = \left\{ 2\gamma_2(L + \Delta z) + \frac{\rho \Delta z L}{2} (V_{FW} + v_a)^2 - \frac{L \Delta z}{2G} (\bar{\mu}_s^2 - \bar{\mu}_d^2) (\rho g H)^2 \right\}$$

$$B_W = L v_a \left(\bar{\mu}_d \rho g H + \eta_e \frac{[V_{FW} + v_a] \cos(\delta)}{\Delta z} \right)$$

In the above expressions, γ_2 is surface-energy density of the felsic shear zone subject to the second-phase along-strike rupture. The general solutions of the above equation are

$$W_m(t) = \frac{A_W W_0}{(A_W + B_W t)}$$

$$\dot{W}_m(t) = -\frac{A_W B_W}{(A_W + B_W t)^2} W_0$$

where $W_0 = W_m(t=0)$ is defined in Eq. (6). Fig. 7 shows how $\dot{W}_m(t=0)$ varies as a function of γ_2 , whereas Fig. 8 shows $\dot{W}_m(t)$ as a linear function of time with the slope depending on shear-zone

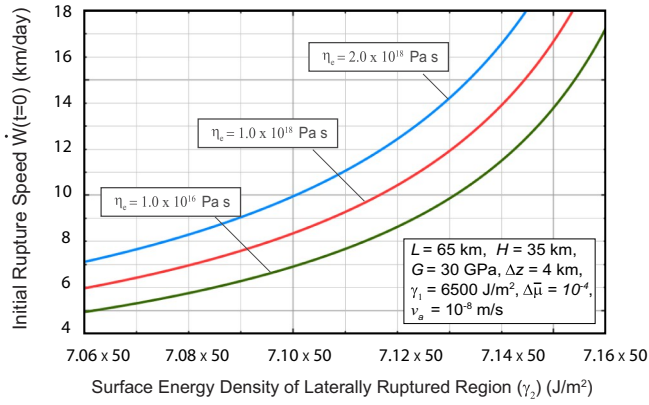


Fig. 7. Initial along-strike rupture speed in the second phase of our kinematic model as a function of surface-energy density of the weaker felsic shear zone. Also shown is the relationship between the initial rupture velocity and the effective viscosity of the weak felsic shear-zone materials.

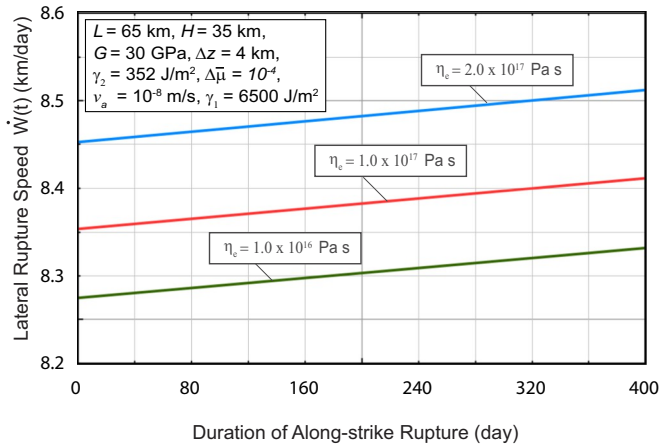


Fig. 8. Along-strike rupture speed as a function of time with variable shear-zone viscosity values.

viscosity. That is,

$$W_m(t) = \epsilon_0(\eta_e)t^2$$

where $\epsilon_0(\eta_e)$ is a function of the effective shear-zone viscosity. The above equation allows us to interpret the physics of Eq. (5c). That is, if a portion of the rupture zone swept by the second-phase rupture consists of multiple dip-parallel lineaments, the width of the corresponding shear-zone segment consisting of mafic lineaments should evolve according to

$$W_d(t) = \epsilon_0(\eta_{e(d)})t^2 \quad (8)$$

where $\eta_{e(d)}$ is the viscosity of the dip-parallel lineaments assumed to be the same. However, the lineament viscosity is different from the felsic-shear-zone viscosity. Hence, a complete absence of dip-parallel lineaments during the second-phase along-strike rupture requires $W_d(t) = 0$. This in turn yields the following two equations:

$$\epsilon_0(\eta_{e(d)}) = 0$$

$$W_e(t) = W_s(t) + W_0 = W_m(t) + W_0$$

The second equation is the same as that shown in Eq. (5b). Insert Eq. (5b) into Eq. (7), we obtain

$$\dot{W}_e(t) + \frac{B_W}{A_W + B_W t} W_e(t) = \frac{B_W}{A_W + B_W t} W_0 \quad (9a)$$

The above equation has the same form as the equation governing

the linear scaling law of Ide et al. (2007). That is,

$$\dot{M}_0(t) = GL\dot{W}_e(t)v_a t + GLW_e(t)v_a = c_0$$

Rearrangement of the above equation leads to

$$\dot{W}_e(t) + \frac{1}{t} W_e(t) = \frac{c_0}{GLv_a t} \quad (9b)$$

where c_0 is the empirical constant in Ide et al.'s linear scaling law in the form of $\dot{M}_0(t) = c_0$. Equating Eqs. (9a) and (9b) yields

$$\frac{B_W}{A_W + B_W t} = \frac{1}{t} \quad (10a)$$

$$c_0 = W_0 GLv_a \quad (10b)$$

Note that W_0 is defined in Eq. (6), which allows us to rewrite the above equation as

$$c_0 = \frac{4\gamma_1 \Delta z G_1 GL^2 v_a}{[L\Delta z(\bar{\mu}_{s1}^2 - \bar{\mu}_{d1}^2)(\rho g H)^2 - 4\gamma_1 G_1(L + \Delta z) - \rho \Delta z L G_1 (V_{FW} + v_a)^2]} \quad (10c)$$

If we further replace v_a by V_{cr} defined in Eq. (2), we get

$$c_0 = \frac{4\gamma_1 \Delta z G_1 GL^2 \left[\frac{(\bar{\mu}_s - \bar{\mu}_d)\rho g H \Delta z}{\eta_e \cos(\delta)} - V_{FW} \right]}{\left[L\Delta z(\bar{\mu}_{s1}^2 - \bar{\mu}_{d1}^2)(\rho g H)^2 - 4\gamma_1 G_1(L + \Delta z) - \rho \Delta z L G_1 \left(\frac{(\bar{\mu}_s - \bar{\mu}_d)\rho g H \Delta z}{\eta_e \cos(\delta)} \right)^2 \right]} \quad (10d)$$

If we assume $G_1 = G$, $\bar{\mu}_s = \bar{\mu}_{s1}$, and $\bar{\mu}_d = \bar{\mu}_{d1}$, Eqs. (10c) and (10d) become

$$c_0 = \frac{4\gamma_1 \Delta z G^2 L^2 v_a}{[L\Delta z(\bar{\mu}_s^2 - \bar{\mu}_d^2)(\rho g H)^2 - 4\gamma_1 G(L + \Delta z) - \rho \Delta z L G (V_{FW} + v_a)^2]} \quad (10e)$$

$$c_0 = \frac{4\gamma_1 \Delta z G^2 L^2 \left[\frac{(\bar{\mu}_s - \bar{\mu}_d)\rho g H \Delta z}{\eta_e \cos(\delta)} - V_{FW} \right]}{\left[L\Delta z(\bar{\mu}_s^2 - \bar{\mu}_d^2)(\rho g H)^2 - 4\gamma_1 G(L + \Delta z) - \rho \Delta z L G \left(\frac{(\bar{\mu}_s - \bar{\mu}_d)\rho g H \Delta z}{\eta_e \cos(\delta)} \right)^2 \right]} \quad (10f)$$

A plot of Eq. (10f) using model parameters appropriate for the Cascadia subduction zone shows that c_0 increases with $(\bar{\mu}_s - \bar{\mu}_d)$ but decreases with η_e (Fig. 9). This result indicates that for the given set of model parameters the denominator in Eq. (10f) changes little, which leads to an approximate scaling relationship of $c_0 \sim \frac{(\bar{\mu}_s - \bar{\mu}_d)}{\eta_e}$. An interesting observation from Eqs. (10e) and (10f) is that c_0 is independent of

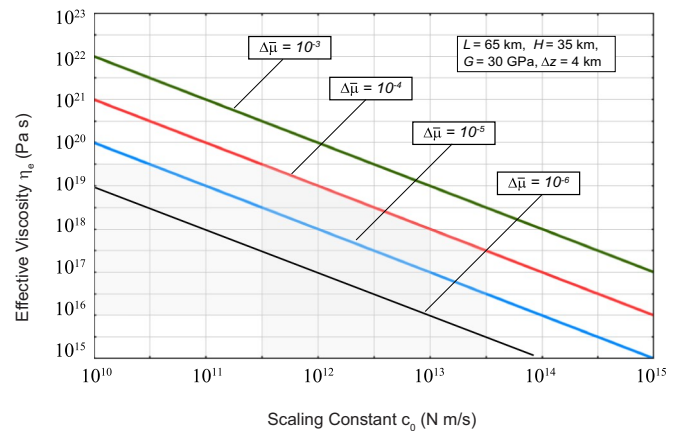


Fig. 9. Relationship between the empirical constant in the linear scaling law of Ide et al. (2007) and the effective shear-zone viscosity as a function of differential friction coefficient.

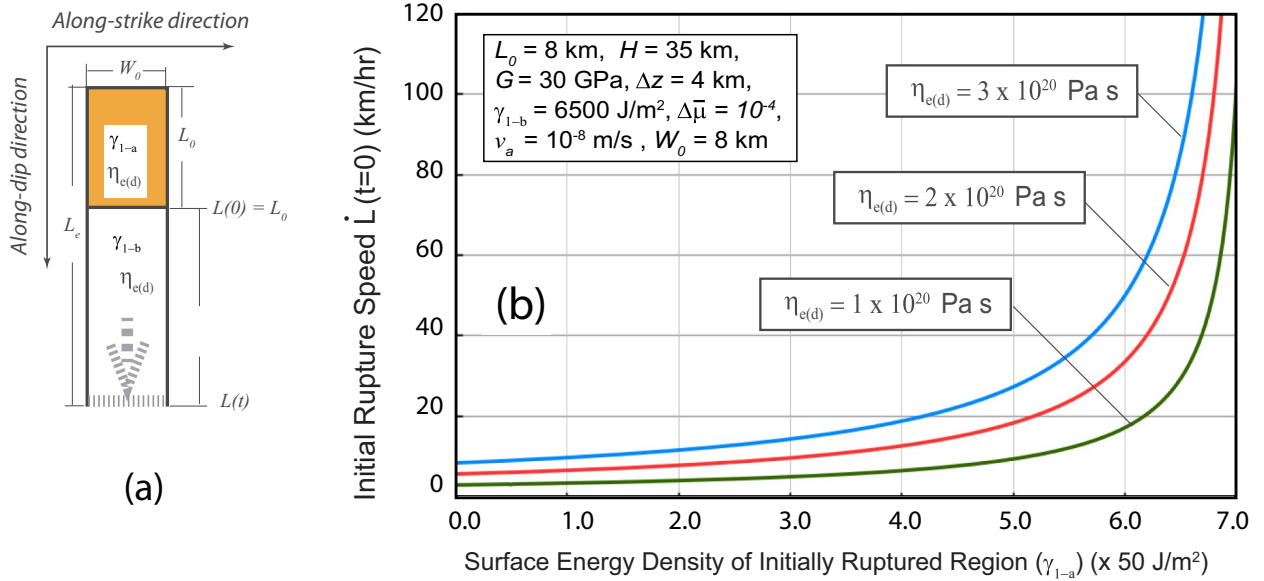


Fig. 10. (A) Geometric parameters of a dip-parallel lineament along which first-phase dip-parallel rupture occurs. (B) The initial dip-parallel rupture speed as a function of surface-energy density and effective viscosity of the mafic lineament. The initial speed is a good proxy of the overall rupture speed during a slow-slip event, as it changes little with time.

the surface-energy density γ_2 for the low-viscosity section of the slow-slip shear zone through which the second-phase along-strike rupture occurs.

If the second-phase along-strike rupture involves multiple dip-parallel mafic lineaments embedded in a felsic matrix, the mechanical properties of the newly ruptured slip zone is no longer homogeneous. In this case, the total width of the mafic lineaments can be expressed as

$$W_d(t) = \epsilon_0(\eta_{e(d)})t^2$$

Using the above relationship, Eq. (3) becomes

$$W_e(t) = W_m(t) + W_0 + \epsilon_0(\eta_{e(d)})t^2$$

Insert the above equation into Eq. (7), we get

$$\dot{W}_e(t) + \frac{B_W}{A_W + B_W t} W_e(t) = \frac{B_W}{A_W + B_W t} (W_0 + \epsilon_0(\eta_{e(d)})t^2) + 2\epsilon_0 t \quad (11)$$

Eq. (11) has a mathematical form for a general scaling law of $\dot{M}_0(t) = c_0(t)$, which can be expressed as a function of the shear-zone geometry (L and W_e), the shear-zone mechanical property (G), and the average slow-slip velocity (v_a) by

$$\dot{M}_0(t) = GL\dot{W}_e(t)v_a t + GLW_e(t)v_a = c_0(t)$$

or

$$\dot{W}_e(t) + \frac{1}{t} W_e(t) = \frac{c_0(t)}{tGLv_a} \quad (12)$$

Equating Eqs. (11) and (12) yields the following two relationships:

$$\frac{B_W}{A_W + B_W t} = \frac{1}{t}$$

$$\frac{c_0(t)}{tGLv_a} = \frac{B_W}{A_W + B_W t} (W_0 + \epsilon_0 t^2) + 2\epsilon_0(\eta_{e(d)})t$$

which in turn requires

$$c_0(t) = GLv_a [W_0 + 3\epsilon_0(\eta_{e(d)})t^2] \quad (13)$$

The above relationship indicates that $\dot{M}_0(t) = c_0(t)$ is scaled to t^2 , which in turn requires

$$M_0(t) \sim t^3.$$

The result shown in Eq. (13) indicates that if the second-phase rupture involves multiple dip-parallel mafic lineaments embedded in an overall felsic shear zone, the scaling relationship between the resulting seismic moment and the event duration should follow a cubic law. Cubic scaling is common for regular earthquakes (Ide et al., 2007) and has been proposed to apply to slow-slip phenomena associated with landslides, strike-slip deformation, and glacial flow (Peng and Gomberg, 2010).

3.4. Finite rupture speed during first-phase slip-zone expansion

We can quantify the first-phase duration and rate of rupture along a dip-parallel high-viscosity mafic lineament using the same physics expressed in Eq. (7). Replace $W_m(t)$ by $L(t)$, we get

$$\dot{L}(t) + \frac{B_L}{A_L + B_L t} L(t) = 0 \quad (14)$$

where

$$A_L = \left\{ 2\gamma_{1-b}(W + \Delta z) + \frac{\rho\Delta z W}{2}(V_{FW} + v_a)^2 - \frac{W\Delta z}{2G}(\bar{\mu}_s^2 - \bar{\mu}_d^2)(\rho g H)^2 \right\}$$

$$B_L = Wv_a \left(\bar{\mu}_d \rho g H + \eta_{e(d)} \frac{[V_{FW} + v_a] \cos(\delta)}{\Delta z} \right)$$

Here, $\eta_{e(d)}$ is the viscosity of the dip-parallel lineament along which initial (=first phase) rupture starts. The initial condition of $L(t=0) = L_0$ must be given in order to solve the above equation. Similar to obtaining W_0 in Eq. (6), we determine L_0 by assuming an instantaneous rupture of a region that has a surface-energy density of γ_{1-a} , a down-dip length of L_0 , and an along-strike width of W_0 . The value of γ_{1-a} differs from the surface-energy density γ_{1-b} for the rest of the high-viscosity strip (Fig. 10a). We assume an instantaneous rupture of a length L_0 (i.e., the 1-a segment in Fig. 10a) followed by rupture of a length $L(t)$ (i.e., the 1-b segment in Fig. 10a) in the dip direction. The two segments of the dip-parallel strip may have different viscosity. For simplicity, we assume that they are the same and expressed as $\eta_{e(d)(1-a)} = \eta_{e(d)(1-b)} = \eta_{e(d)}$. For $W_0 = 10$ km and $L_0 = 8$ km, an initial rupture speed of 60–120 km can be achieved when $\gamma_{1-a} \leq 350$ J m⁻² and $\eta_{e(d)} > 10^{20}$ Pa s (Fig. 10b). Not shown here is the time evolution of the along-dip rupture speed, which changes little from the initial

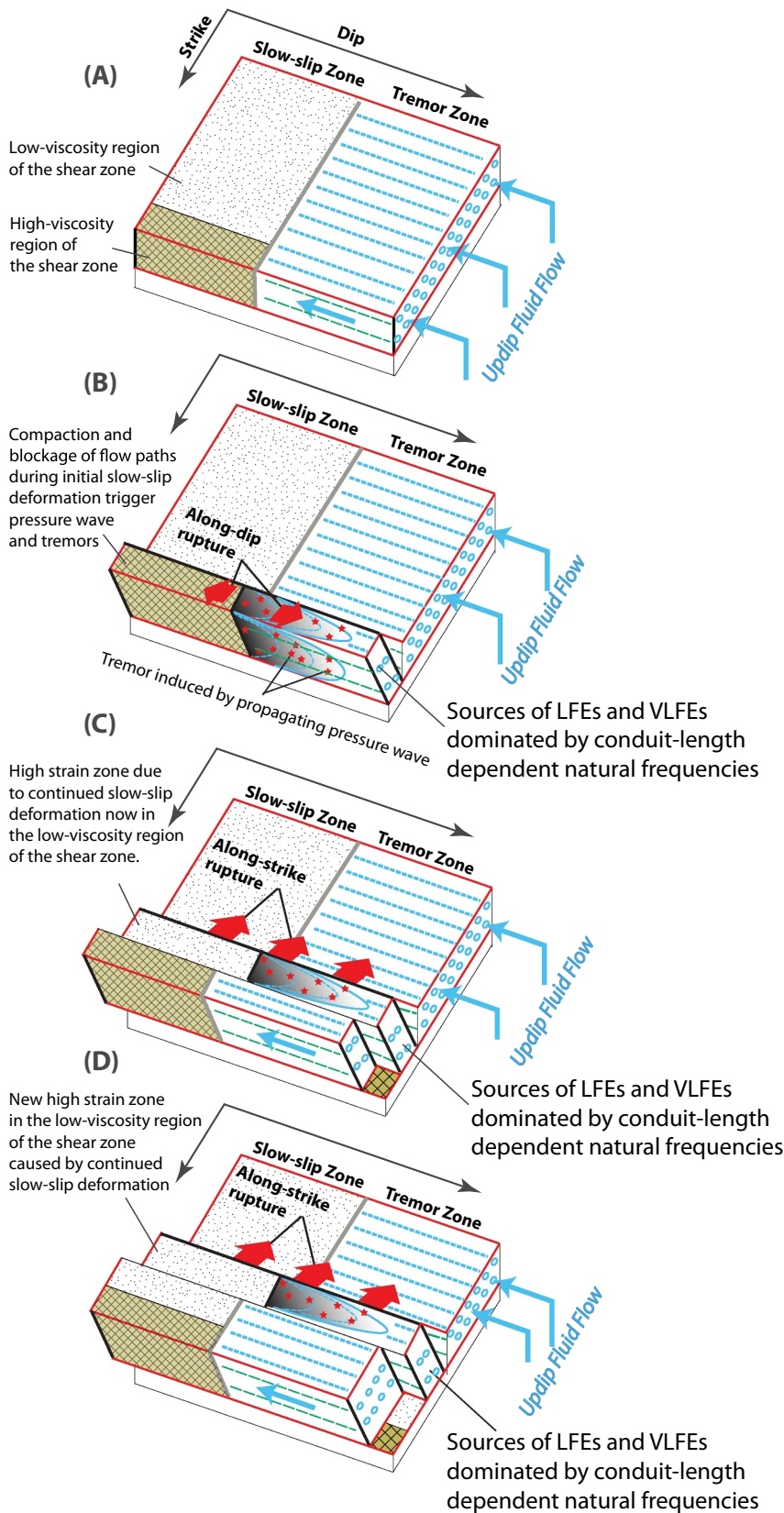


Fig. 11. (A) The initial state of a seismic-aseismic transition zone consisting of an updip slow-slip shear zone and a downdip tectonic-tremor zone. The slow-slip zone consists of a high-viscosity dip-parallel mafic lineament along which rupture starts. The length of the lineament guides a constant-length expansion of the rupture zone in the strike direction. (B) Compaction (i.e., volume reduction) and resulting sudden blockage of porous conduits with moving pore-fluids generate a propagating pressure wave along the mafic lineament. Although we show here that a propagating pressure wave triggers migrating tremors in the downdip direction, the tremor migration could be bidirectional from a point or in the updip direction depending on the strength distribution and magnitude of the elevated pore-fluid pressure induced by the pressure wave. (C) Stress concentration along the dip-parallel edges of the early ruptured strip following the mafic lineament creates high strain along the margins of the neighboring felsic shear zone. Compaction by the high-strain deformation is capable of causing sudden blockage of flow paths along porous conduits. This in turn triggers propagating pressure wave and progressive shear failure along the wave paths expressed as migrating tectonic tremors. (D) A new high-strain zone along the edges of newly ruptured area causes tectonic compaction, which again triggers conduit-guided pressure waves and migrating tectonic tremors along the wave paths.

rupture speed with time. The results shown in Fig. 10b imply that the initially ruptured region may be highly fractured as required by the low surface-energy density.

Fig. 10b also shows that the required shear-zone viscosity for high-speed rupture is about 2–4 orders of magnitude higher than the bulk

viscosity of deep subduction slow-slip shear zones, inferred from slow-slip durations, slow-slip magnitudes, and after-slip deformation history between 10^{16} and 10^{18} Pa s (Hu et al., 2016; Yin et al., 2018). This difference is also evident by comparing Fig. 10b against Fig. 9; for $\Delta\bar{\mu} = 10^{-5}$ and c_0 between $10^{11.5}$ and $10^{13.5}$ N m s⁻¹ as shown in Fig. 1b;

the required bulk shear-zone viscosity is lower and between $10^{16.5}$ Pa s and $10^{18.5}$ Pa s.

4. Discussion

Two prominent issues with regard to slow-slip scaling have been debated: (a) what does the empirical constant c_0 mean physically? and (b) why do fast and slow earthquakes scale differently (but see discussion by Peng and Gomberg, 2010 and Gomberg et al., 2016)? While there had been no analytical expression of c_0 derived from the first principles, several end-member models have been proposed to explain the linear slow-slip scaling and its difference from regular earthquake scaling. These include (1) a diffusion-like rupture process (Ide et al., 2007), (2) a stochastically varying source area during a slow slip event (Ide, 2008, 2010; Ide and Maury, 2018), (3) bounded versus unbounded elastic dislocation (Gomberg et al., 2016), and (4) rate-state friction with the consideration of (i) a cutoff velocity (Colella et al., 2011, 2013; Shibasaki et al., 2012), (ii) slip-front interactions (Liu, 2014), (iii) multi-fault interaction (Romanet et al., 2018), or (iv) energy consumption by plastic deformation (Tong and Lavier, 2018). In this study, we show that the linear slow-slip scaling can be achieved if a slow-slip shear zone consists of a high-viscosity mafic lineament in an overall felsic low-viscosity matrix. Such an anisotropy can lead to an early rupture along the strong mafic lineament at a fast speed and a later along-strike rupture propagating through the felsic shear zone at a much slower speed. When energy balance during slow-slip deformation is considered, the above process leads to an analytical form of the observed linear scaling law that relates the empirical scaling constant to the geometric, kinematic, and mechanical properties of a deep-subduction slow-slip shear zone. An important implication of our model is that the presence of a strong dip-parallel lineament dictates how a rupture process evolves and how seismic moments may scale with event durations. We speculate that a similar physics may also apply to large ($M_w > 7.5$) fast earthquakes along oceanic and continental subduction zones, which also display slow along-strike rupture during the later phase of the recorded seismic events (e.g., Simons et al., 2011; Avouac et al., 2015). Below we discuss the implications and limitations of the model presented in this study.

4.1. Linear, nonlinear, or continuum scaling

Peng and Gomberg (2010) proposed that slow-slip earthquakes from a full spectrum of tectonic (i.e., strike-slip faults and subduction zones) and non-tectonic (landslides and glacier deformation) settings should follow a continuum scaling law, which are bounded by $M_0 \sim T$ and $M_0 \sim T^3$. In our data synthesis shown in Fig. 1b, we find that this is clearly not the case for deep subduction slow-slip events and tectonic tremors. Assuming a saturation frequency that limits the apparent corner frequency value, Bostock et al. (2015, 2017) found that the tectonic tremors at the Cascadia convergent margins follow a scaling relationship of $M_0 \sim T^{1/10}$. However, it is unclear whether this new scaling law is a result of their specific data-processing methods (cf., Hawthorne and Bartlow, 2018).

As shown in our derivation, a linear scaling relationship is achievable when the along-strike rupture occurs entirely in a homogeneous shear zone without involvement of dip-parallel seamount-induced mafic lineaments. In contrast, a cubic scaling relationship can be obtained when along-strike rupture encounters multiple dip-parallel mafic lineaments. The two scaling relationships we obtained, resulting from two different mechanical properties of a slow-slip shear zone, represent the upper and lower bounds of the continuum scaling law of Peng and Gomberg (2010). The lack of a cubic-law expression of deep subduction slow-slip events in Fig. 1b indicates that large-scale lineaments created by seamount subduction are rarely encountered by lateral rupture of individual slow-slip events.

4.2. Relationship between aseismic slow-slip and seismic tremors

In light of our model results and inspired by the early work of Ghosh et al. (2010) and Frank et al. (2015), we suggest a possible model that relates slow-slip deformation to tectonic tremors during a deep (15–50 km) subduction slow-slip event. Fig. 11a shows an end-member case in which the slow-slip and tectonic-tremor zones are separated along a seismic-aseismic transition zone at a convergent margin. The two sub-zones could overlap, which does not change the nature of a conceptual model presented below.

We envision that the slow-slip and tectonic-tremor zones both consist of dip-parallel lineaments serving as fluid-transport conduits. However, we suggest that the larger-scale mafic lineaments created by seamount subduction are concentrated in the slow-slip shear zone (see Fig. 2a), whereas the finer-scale mafic lineaments expressed as stretching lineations and strips of mafic and ultramafic bodies at scales of a few meters to 100 m are concentrated in the tremor zones (Fig. 11a) (also see Fig. 3). The stress-guide effect of a strong and larger-scale mafic lineament localizes the initial rupture as a narrow dip-parallel strip (Fig. 11b). The rupture speed along the stress guide is fast due to its high viscosity as shown in our model. Based on the experimental results of Violay et al. (2015) on porosity evolution of mafic rocks under brittle-ductile-transition conditions, we expect that the initial deformation of the mafic stress guide is compactional (i.e., volume reduction assuming that new pore space forms constantly between slow-slip events induced by dehydration reactions and hydraulic fracturing). This in turn can cause sudden blockage of up-dip pore-fluid flow paths along the slow-slip shear zone. The conduit blockage would trigger a propagating pressure wave from the blocking site, causing progressive plastic failure of the shear zone due to elevated pore-fluid pressure associated with the wave. The wave propagation is then expressed as migrating tectonic tremors in the dip-parallel direction (Fig. 11b) (Yin, 2018). The fast speed tremor migration (~ 100 km/h) is the same as the speed of the propagating pressure wave in the tremor zone. Deformation by slow-slip and tremor activities created the initially ruptured area along the mafic lineament as shown in Fig. 11c. Continued slow-slip deformation creates high strain along the dip-parallel edges of the initially ruptured mafic strip, which lies against the neighboring low-viscosity felsic shear zone (Fig. 11c). The slow converting rate from elastic energy to viscoplastic dissipation through the low-viscosity felsic shear zone is expressed by a much slower rupture speed (i.e., 5–10 km/day for a shear zone with a viscosity of 10^{16} to 10^{17} Pa s as shown in our model) as the slip-area expands laterally. Slow-slip deformation of the felsic shear zone is also expected to be compactional as indicated by the experimental results of Violay et al. (2017) for granitic rocks under brittle-ductile-transition conditions. This may cause sudden blockage of pore-fluid conduits, which in turn can trigger a propagating pressure wave. Again, the pressure wave with an elevated pore-fluid pressure is capable of inducing progressive shear failure expressed as migrating tectonic tremors (Fig. 11c). Once the stress along the edges of the newly ruptured dip-parallel strip in the felsic shear-zone exceeds the rock plastic strength, rupture propagates laterally in the strike direction (Fig. 11d). Repeating the above processes leads to continued along-strike expansion of the slip area.

Although both the fault-valve model of Frank et al. (2015) and the pressure-wave model of Yin (2018) involve pore-fluid pressure propagation, the two mechanisms predict very different physical processes (also see Shapiro et al., 2018). In the Frank et al. (2015) model, tremors were induced by diffusive pore-fluid flow, whereas in the Yin (2018) model, fluid pressure is transmitted by an acoustic wave. For a pore-fluid viscosity of 10^{-3} Pa s, a shear-zone permeability of 10^{-13} m², and pore-fluid flow driven by a lithostatic pressure gradient, the resulting Darcy's flow rate is $\sim 10^{-6}$ km/h, which is too slow to explain the propagation speed of tremors migrating on the order of ~ 100 km/h in the dip direction. In contrast, the pressure-wave model does not require a fast moving fluid flow. Under this mechanism, the acoustic vibration

of fluid-filled porous bodies transmits an elevated pore-fluid pressure along the propagating pressure-wave path. As pressure waves can also be generated in slow-slip shear zones by tectonic compaction, the absence of tremors in the shear zones requires an explanation. It is possible that the plastic yield strength of slow-slip shear zones is too high to fail plastically triggered by the wave-generated pore-fluid pressure. This explanation is problematic as motion along slow-slip shear zones is well recorded during slow-slip events, which indicates that the stress magnitude is sufficient to initiate slip motion. A more likely explanation is that the *higher viscosity* of an updip slow-slip shear zone than that of a downdip tectonic-tremor zone leads to two consequences: (1) a stronger viscous damping in the colder slow-slip shear zone that may prevent the occurrence of a pressure wave, and (2) stronger reduction of natural frequency by viscous damping makes slow-slip events as *extremely low frequency* earthquakes detectable only geodetically.

In theory, a sudden blockage of a porous conduit with moving pore-fluid generates pressure waves that can propagate in the opposite direction from a blockage site. This is because a sudden stopping of a moving fluid creates an increase in fluid pressure on the upstream side and a decrease in fluid pressure on the downstream side of the blockage site; both the sudden reduction and generation of pore-fluid pressure can generate pressure waves (e.g., Ghidaoui et al., 2005). For rocks with a single lithology, the plastic yield strength under the brittle and brittle-ductile-transition conditions decreases with increasing temperature (e.g., Violay et al., 2015; Pec et al., 2016; French and Zhu, 2017). This well-known experimental result implies that the downdip propagating pressure wave is more favorable to trigger migrating tremors as shown in Fig. 11. However, the observed migration directions of tremors are both updip and downdip (Ghosh et al., 2010), which require other factors such as complex lithologies and the pressure effects to dictate the spatial distribution of rock strengths along a tectonic-tremor zone.

A simple extension of the conceptual model shown in Fig. 11 may explain the occurrences of rapid tremor reversals (Houston et al., 2011). That is, a sudden release of fluid from a pressurized dip-parallel linear body with a high porosity may trigger a pressure wave into the newly ruptured slip zone (Fig. 12). The pressure-wave model may also explain the observed back-and-forth migrating tremors along the same path during a single slow-slip event Ghosh et al. (2010), resulting from reflection waves along a linear porous body as shown in Fig. 12.

4.3. Origin of low frequency and very lower frequency earthquakes

Tremors are interpreted to consist of a group of individual LFEs and

very low frequency earthquakes (VLFs) and are recorded on seismic instruments, proving that they result from seismic radiations. For instance, along the central San Andreas fault near Parkfield, the tremors exhibit a continuum feature with regular earthquakes, which are located on the same fault plane at different depths (Shelly and Hardebeck, 2010). Using a phase-weighted stacking technique, low-frequency earthquakes within tectonic tremors at the Cascadia margin are stacked to enhance the signal-noise-ratio, which display impulsive *P* waves (Thurber et al., 2014). This indicates that tectonic tremors are induced by shear deformation similar to regular earthquakes, but somehow they lack high-frequency radiation comparing with regular earthquakes of similar sizes. Similarly, VLFs seen from records of seismographs have also been interpreted to represent seismic-energy radiation from the source (e.g., Ito and Obara, 2006). Consistent with the above interpretations, Yin (2018) suggested that the low and very low frequencies of tectonic tremors are dominated by resonance frequencies controlled mainly by the length of linear fluid-filled porous conduits in slow-slip shear zones (also see Fig. 11). As mentioned above, the characteristically low to very low frequencies of the tectonic tremors could also be induced by viscous damping, which has the strongest effect on an updip higher-viscosity slow-slip shear zone with a lower average temperature than that on a downdip lower-viscosity tremor zone with a higher average temperature.

4.4. Model limitations

Unlike most numerical models whose results are rarely verified by other independent researchers, our analytical solution can be easily inspected and validated. However, the simplicity of our model comes at the expense of several critical assumptions and their impacts and limitations are discussed below. First, we assume two-stage rupture during a slow-slip event based on the observed tremor migration patterns and geodetic inversion results (Shelly et al., 2007; Ghosh et al., 2010; Bartlow et al., 2011, 2014; Bletery et al., 2017). As this kinematic process is *ad hoc*, a more holistic study without involving an assumed rupture kinematic model is needed.

Second, our model treats a slow-slip shear zone to have a uniform static strength and a uniform dynamic strength. Such an assumption is valid only if the slow-slip shear zone is horizontal and the shear-zone pore-fluid pressure has no spatial variation. This assumption may be valid for the case of the southern Mexico subduction zone (Frank et al., 2015), but does not hold for other convergent margins that generate slow-slip events. As slow-slip subduction zones all have rather gentle dip angles ($< 15^\circ$) (e.g., Schwartz and Rokosky, 2007) and pore-fluid

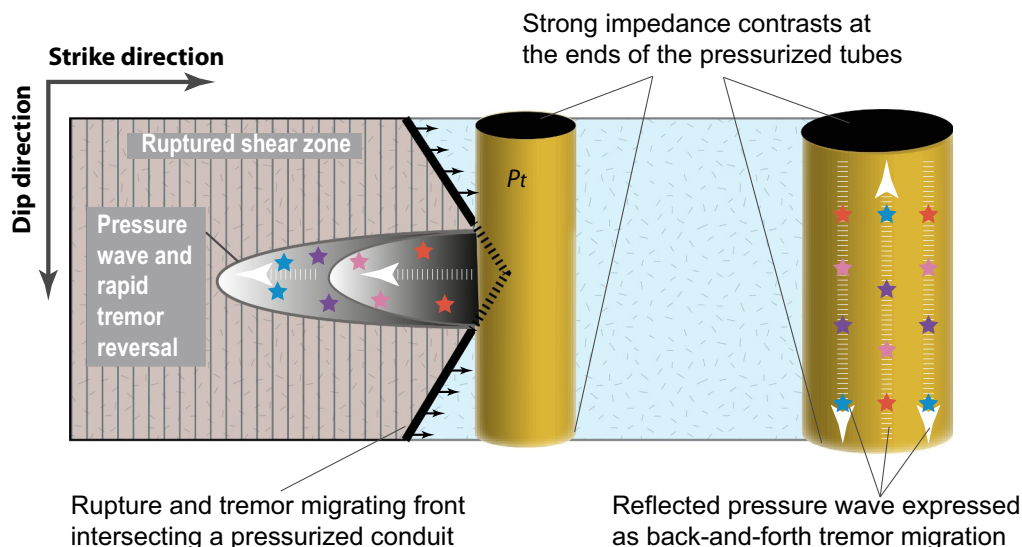


Fig. 12. A conceptual model illustrating the generation of rapid tremor reversal (RTR) of Houston et al. (2011) during lateral along-strike propagation of a rupture front. In this model, RTRs were generated by a sudden release of pore-fluid jets into the newly ruptured area from a linear, pressurized, and dip-parallel high-porosity body. Also shown is a possible scenario that explains the observed back-and-forth tremor migrations along the same path with the same path travel times as observed by Ghosh et al. (2010). Here, reflection of pressure waves causes back-and-forth migrating tremors along a tube-like porous body.

pressures close to the lithostatic-pressure values (e.g., Audet and Schaeffer, 2018), our assumed uniform shear-zone strengths should be an adequate first-order approximation.

Third, the assumed instantaneous strength drop at the onset of a slow-slip event requires velocity weakening, which is predicted by rate-state friction laws (e.g., Segall et al., 2010; Chen et al., 2017) but not incorporated in our model explicitly. Despite this shortcoming, we suggest that the velocity-weakening process immediately before the onset of a slow-slip event occurs in brittle mafic materials embedded in an overall ductile felsic shear zone. As shown experimentally, a pure mafic rock, such as gabbro, displays an unstable sliding behavior under brittle-ductile-transition conditions relevant to deep slow-slip deformation (He et al., 2007). In contrast, mafic rocks mixed with a small amount of quartz under the same conditions exhibit a velocity-strengthening effect (He et al., 2013). Here, we suggest that the experimental results of He et al. (2007) using only mafic materials may capture the mechanical behavior immediately prior to the onset of a slow-slip event not considered in our model, whereas the results of He et al. (2013) involving a mixture of mafic brittle and felsic ductile materials may represent the mechanical behavior of viscoplastic deformation quantified in our model.

Fourth, the derivation of our scaling relationships is based on an energy-balance relationship during slow-slip deformation that neglects the effect of seismic-energy radiation. As a result, our model should be applicable only to aseismic slow-slip processes that do not involve tectonic tremors.

Fifth, our model assumes a linear viscoplastic rheology, which implies that the shear-zone viscosity is independent of slip velocity and strain rate. This assumption may be valid if diffusion-controlled crystal-plastic deformation dominates during deep subduction slow-slip deformation (Kohlstedt et al., 1995). Indeed, Audet and Bürgmann (2014) show that precipitation and dissolution may have played a controlling role in dictating the strength and stress state of deep subduction slow-slip shear zones. However, this inference does not rule out the possibly coeval operation of several deformation mechanisms under the brittle-ductile transition conditions for a shear zone with a diverse lithology (e.g., Chester, 1995; Pec et al., 2016; Platt et al., 2018; Goswami and Barbot, 2018).

Finally, the rock volume considered in our energy balance equation only involves elastic deformation of the slow-slip shear zone. In reality, the storing volume of elastic energy may be much larger, perhaps

Appendix

A.1. Initial shear-zone width W_0

The instantaneously formed initial dip-parallel rupture-zone has a width W_0 , which is shown in Eq. (6). Its derivation is based on the following assumptions:

- (1) The initial shear zone has a constant down-dip length L and a constant thickness Δz , same as the rest of the shear zone that may have different rheological properties.
- (2) The elastic energy of the shear zone and the kinetic energy of the moving hanging wall must be balanced by non-elastic dissipation over the shear-zone volume during a slow-slip event (e.g., Anderson, 2005).
- (3) The non-elastic dissipation includes viscoplastic deformation and creation of new slip surfaces assumed to be along the bounding planes of the shear-zone volume only. In the derivation below, we neglect seismic radiation.
- (4) The release of elastic energy is determined by shear stress drop from the static plastic strength (Y_s) to the dynamic plastic strength (Y_d).
- (5) The release history of elastic energy, denoted as $\Delta U_i(t)$, varies with time due to lateral expansion of the rupture zone $W(t)$ that has a constant dip-parallel length L and a constant shear zone thickness Δz .

For a slow-slip event along a viscoplastic shear zone that has static and dynamic yield strengths and a constant effective viscosity, the energy-release history, energy-rate history, and initial condition of the elastic energy can be expressed in the following three equations:

$$\Delta U_i(t) = -W(t) \frac{L\Delta z}{G} \int_{Y_s}^{Y_d} \tau_e d\tau_e = W(t) \frac{L\Delta z}{2G} (Y_s^2 - Y_d^2) \quad \text{Elastic Energy Release History} \quad (\text{A1a})$$

involving the regions directly above the slow-slip shear zone and beyond. However, we do not believe that this would fundamentally change the conclusions reached in this study.

5. Conclusions

In this study, we address the questions of what controls the linear slow-slip scaling between seismic moments and event durations and the cause of anisotropic slow-slip rupture speeds along deep (15–50 km) subduction shear zones. Based on geologic constraints, we treat slow-slip shear zones to be anisotropic and viscoplastic. The anisotropy is due to the presence of dip-parallel (= slip-parallel) high-viscosity mafic lineaments derived from subduction of seamounts, which are embedded in an overall felsic low-viscosity slow-slip shear zone. The viscoplasticity is due to deformation of mixed brittle mafic and ductile felsic rocks in the shear zone. We postulate that the shear-zone anisotropy controls the following commonly observed slow-slip rupture pattern: initial along-dip rupture along a high-viscosity mafic lineament followed by along-strike expansion of the early ruptured strip through the felsic shear zone. By combing this two-stage rupture model with an energy balance equation, we derive an analytical expression of the empirically observed scaling law first proposed by Ide et al. (2007). Our analytical solution indicates that the empirical scaling constant depends on the geometric, kinematic, and mechanical properties of a deep subduction slow-slip shear zone. Our model can also lead to the derivation of a cubic scaling law under the condition that the along-strike rupture involves multiple dip-parallel high-viscosity mafic lineaments. Finally, our anisotropic shear-zone model predicts fast (~ 100 km/h) rupture in the dip direction along a high-viscosity (10^{20} Pa s) mafic lineament and slow (2–10 km/day) rupture in the strike direction propagating through a low-viscosity (10^{17} Pa s) felsic shear zone.

Acknowledgements

We thank Dr. Jianye Chen for his comments on an early draft of this work. The manuscript would not reach its current form without the thoughtful comments by an anonymous journal reviewer. This work is strongly inspired by the work of Abhijit Ghosh at UCLA and Heidi Houston at USC. We thank Lingsen Meng, Paul Davis, William Frank, Heidi Houston, and Yehuda Ben-Zion for stimulating discussions throughout the course of this research.

$$\Delta \dot{U}_i(t) = \dot{W}(t) \frac{L\Delta z}{2G} (\bar{\mu}_s^2 - \bar{\mu}_d^2)(\rho g H)^2 \quad \text{Elastic Energy Release Rate History} \quad (\text{A1b})$$

$$\Delta U_i(0) = W(0) \frac{L\Delta z}{2G} (\bar{\mu}_s^2 - \bar{\mu}_d^2)(\rho g H)^2 \quad \text{Initial Condition} \quad (\text{A1c})$$

where $Y_s = \bar{\mu}_s \rho g H$ and $Y_d = \bar{\mu}_d \rho g H$, with $\bar{\mu}_s$ and $\bar{\mu}_d$ representing effective coefficients of static and dynamic friction, ρ rock density, g gravitational acceleration, and H averaged depth to the shear zone. Here, we assign $W = W_m$.

The surface-energy evolution history, surface-energy rate history, and initial surface energy of a six-sided shear zone (Δz , L , and $W(t)$), can be written as (again note that $W = W_m$)

$$R_S(t) = 2\gamma_1 L W(t) + 2\gamma_1 L \Delta z + 2\gamma_1 W(t) \Delta z \quad \text{Surface Energy History} \quad (\text{A2a})$$

$$\dot{R}_S(t) = \dot{W}(t) \gamma_1 (2L + 2\Delta z) \quad \text{Surface Energy Rate History} \quad (\text{A2b})$$

$$R_S(t=0) = R_S(0) = W(t=0) 2\gamma_1 (L + \Delta z) + 2\gamma_1 L \Delta z \quad \text{Initial Condition} \quad (\text{A2c})$$

where γ_1 is surface-energy density consumed by seismic radiation and creation of a new slip surfaces. The initial width of the shear zone is denoted as $W(t=0) = W_0$.

The kinetic energy, energy rate, and initial energy at the onset of a slow-slip event with a constant hanging-wall slip velocity v_a can be written as

$$R_k(t) = W(t) \frac{\rho \Delta z L}{2} (V_{FW} + v_a)^2 \quad \text{Kinetic Energy History} \quad (\text{A3a})$$

$$\dot{R}_k(t) = \dot{W}(t) \frac{\rho \Delta z L}{2} (V_{FW} + v_a)^2 \quad \text{Kinetic Energy Rate History} \quad (\text{A3b})$$

$$R_k(t=0) = R_k(0) = W(0) \frac{\rho \Delta z L}{2} [V_{FW} + v_a]^2 \quad \text{Initial Condition} \quad (\text{A3c})$$

where V_{FW} is the subducting-plate velocity relative to the stable interior of the overriding plate.

The resisting viscoplastic dissipation, dissipation rate, and the initiate dissipation can be expressed as

$$\begin{aligned} R_{vp}(t) &= W(t) \Delta z L \int_0^t \tau_{vp} d\varepsilon_{vp} \\ &= W(t) \Delta z L \left(\bar{\mu}_d \rho g H + \eta_e \frac{[V_{FW} + v_a]}{\Delta z} \right) \frac{v_a}{\Delta z} t \quad \text{Dissipation History} \end{aligned} \quad (\text{A4a})$$

$$\dot{R}_{vp}(t) = [\dot{W}(t)t + W(t)] L \left(\bar{\mu}_d \rho g H + \eta_e \frac{[V_{FW} + v_a]}{\Delta z} \right) v_a \quad \text{Dissipation Rate History} \quad (\text{A4b})$$

$$R_{vp}(0) = 0 \quad \text{Initial Condition} \quad (\text{A4c})$$

where $\tau_{vp} = \bar{\mu}_d \rho g H + \eta_e \frac{[V_{FW} + v_a] \cos(\delta)}{\Delta z}$ is the shear stress in the viscoplastic shear zone during a slow-slip event, $\varepsilon_{vp} = \frac{v_a}{\Delta z} dt$ is the viscoplastic shear strain, and η_e is the effective shear-zone viscosity.

At $t = 0$, we have $\Delta U_i(0) = R_S(0) + R_k(0) + R_{vp}(0)$, which leads to

$$W_0 = \frac{2\gamma_1 L \Delta z}{\left[\frac{L\Delta z}{2G} (\bar{\mu}_s^2 - \bar{\mu}_d^2)(\rho g H)^2 - 2\gamma_1 (L + \Delta z) - \frac{\rho \Delta z L}{2} [V_{FW} + v_a]^2 \right]} \quad (\text{A5})$$

As $W_0 > 0$, γ_1 must be smaller than a critical value, which can be derived from Eq. (A5) as

$$\gamma_{1-max} = \frac{L\Delta z [(\bar{\mu}_s^2 - \bar{\mu}_d^2)(\rho g H)^2 - G\rho(V_{FW} + v_a)^2]}{4G_2(L_2 + \Delta z)}$$

To distinguish the mechanical properties of an initially ruptured dip-parallel strip with a width of W_0 along a mafic lineament from the rest of the felsic shear zone, we rewrite Eq. (A5) as

$$W_0 = \frac{4\gamma_1 G_1 L \Delta z}{\left[L\Delta z (\bar{\mu}_{s1}^2 - \bar{\mu}_{d1}^2)(\rho g H)^2 - 4\gamma_1 G_1 (L + \Delta z) - \rho \Delta z L G_1 (V_{FW} + v_a)^2 \right]} \quad (\text{A6})$$

where subscript 1 represents mechanical properties of the initially ruptured mafic strip that differ from the rest of the shear zone. The above equation is Eq. (6) in the main text.

A.2. Along-strike rupture through a homogeneous viscoplastic shear zone

We assume that along-strike rupture is governed by the balance of energy rate (e.g., [Anderson, 2005](#)) during a slow-slip event. This statement can be expressed as

$$\Delta \dot{U}_i(t) = \dot{R}_S(t) + \dot{R}_k(t) + \dot{R}_{vp}(t) \quad (\text{A7})$$

Each term in the above equation is defined from Eqs. (A1) to (A4). After some algebra and letting $W(t) = W_m(t)$, Eq. (A7) becomes

$$\dot{W}_m(t) + \frac{B_W}{A_W + B_W t} W_m(t) = 0 \quad (\text{A8})$$

which is the same equation as that shown in Eq. (7) in the main text, where

$$A_W = \left\{ 2\gamma_2(L + \Delta z) + \frac{\rho\Delta zL}{2}(V_{FW} + v_a)^2 - \frac{L\Delta z}{G}(\bar{\mu}_s^2 - \bar{\mu}_d^2)(\rho gH)^2 \right\} \quad (\text{A9a})$$

$$B_W = Lv_a \left(\bar{\mu}_d \rho gH + \eta_e \frac{[V_{FW} + v_a] \cos(\delta)}{\Delta z} \right) \quad (\text{A9b})$$

The general solutions of Eq. (A8) are

$$W(t) = \frac{A_W W_0}{(A_W + B_W t)} \quad (\text{A10a})$$

$$\dot{W}(t) = -\frac{A_W B_W}{(A_W + B_W t)^2} W_0 \quad (\text{A10b})$$

where $W_0 = W(t=0)$ is defined in Eq. (A5).

References

- Aki, K., 1967. Scaling law of seismic spectrum. *J. Geophys. Res.* 72 (4), 1217–1231.
- Anderson, T.L., 2005. *Fracture Mechanics: Fundamentals and Applications*. CRC press (630 pp).
- Ando, R., Nakata, R., Hori, T., 2010. A slip pulse model with fault heterogeneity for low-frequency earthquakes and tremor along plate interfaces. *Geophys. Res. Lett.* 37 (10).
- Araki, E., Saffer, D.M., Kopf, A.J., Wallace, L.M., Kimura, T., Machida, Y., Ide, S., Davis, E., Expedition, I.O.D.P., 2017. Recurring and triggered slow-slip events near the trench at the Nankai Trough subduction megathrust. *Science* 356 (6343), 1157–1160.
- Audet, P., Bürgmann, R., 2014. Possible control of subduction zone slow-earthquake periodicity by silica enrichment. *Nature* 510 (7505), 389.
- Audet, P., Schaeffer, A.J., 2018. Fluid pressure and shear zone development over the locked to slow slip region in Cascadia. *Sci. Adv.* 4 (3), eaar2982.
- Avouac, J.P., Meng, L., Wei, S., Wang, T., Ampuero, J.P., 2015. Lower edge of locked Main Himalayan Thrust unzipped by the 2015 Gorkha earthquake. *Nat. Geosci.* 8 (9), 708.
- Bartlow, N.M., Miyazaki, S.I., Bradley, A.M., Segall, P., 2011. Space-time correlation of slip and tremor during the 2009 Cascadia slow slip event. *Geophys. Res. Lett.* 38 (18).
- Bartlow, N.M., Wallace, L.M., Beavan, R.J., Bannister, S., Segall, P., 2014. Time-dependent modeling of slow slip events and associated seismicity and tremor at the Hikurangi subduction zone, New Zealand. *J. Geophys. Res. Solid Earth* 119 (1), 734–753.
- Bebout, G.E., Barton, M.D., 2002. Tectonic and metasomatic mixing in a high-T, subduction-zone mélange—insights into the geochemical evolution of the slab–mantle interface. *Chem. Geol.* 187 (1–2), 79–106.
- Behr, W.M., Kotowski, A.J., Ashley, K.T., 2018. Dehydration-induced rheological heterogeneity and the deep tremor source in warm subduction zones. *Geology* 46 (5), 475–478.
- Beroza, G.C., Ide, S., 2011. Slow earthquakes and nonvolcanic tremor. *Annu. Rev. Earth Planet. Sci.* 39, 271–296.
- Bletery, Q., Thomas, A.M., Hawthorne, J.C., Skarbek, R.M., Rempel, A.W., Krogstad, R.D., 2017. Characteristics of secondary slip fronts associated with slow earthquakes in Cascadia. *Earth Planet. Sci. Lett.* 463, 212–220.
- Bostock, M.G., Thomas, A.M., Savard, G., Chuang, L., Rubin, A.M., 2015. Magnitudes and moment-duration scaling of low-frequency earthquakes beneath southern Vancouver Island. *J. Geophys. Res. Solid Earth* 120 (9), 6329–6350.
- Bostock, M.G., Thomas, A.M., Rubin, A.M., Christensen, N.I., 2017. On corner frequencies, attenuation, and low-frequency earthquakes. *J. Geophys. Res. Solid Earth* 122 (1), 543–557.
- Bürgmann, R., 2018. The geophysics, geology and mechanics of slow fault slip. *Earth Planet. Sci. Lett.* 495, 112–134.
- Chen, J., Niemeijer, A.R., Spiers, C.J., 2017. Microphysically derived expressions for rate-and-state friction parameters, a , b , and Dc . *J. Geophys. Res. Solid Earth* 122 (12), 9627–9657.
- Chester, F.M., 1995. A rheologic model for wet crust applied to strike-slip faults. *J. Geophys. Res. Solid Earth* 100 (B7), 13033–13044.
- Cloos, M., 1992. Thrust-type subduction-zone earthquakes and seamount asperities: a physical model for seismic rupture. *Geology* 20 (7), 601–604.
- Colella, H.V., Dieterich, J.H., Richards-Dinger, K.B., 2011. Multi-event simulations of slow slip events for a Cascadia-like subduction zone. *Geophys. Res. Lett.* 38 (16).
- Colella, H.V., Dieterich, J.H., Richards-Dinger, K., 2013. Spatial and temporal patterns of simulated slow slip events on the Cascadia megathrust. *Geophys. Res. Lett.* 40 (19), 5101–5107.
- Denolle, M.A., Shearer, P.M., 2016. New perspectives on self-similarity for shallow thrust earthquakes. *J. Geophys. Res. Solid Earth* 121 (9), 6533–6565.
- Dragert, H., Wang, K., 2011. Temporal evolution of an episodic tremor and slip event along the northern Cascadia margin. *J. Geophys. Res. Solid Earth* 116 (B12).
- Dragert, H., Wang, K., James, T.S., 2001. A silent slip event on the deeper Cascadia subduction interface. *Science* 292 (5521), 1525–1528.
- Duan, B., 2012. Dynamic rupture of the 2011 Mw 9.0 Tohoku-Oki earthquake: Roles of a possible subducting seamount. *J. Geophys. Res. Solid Earth* 117 (B5).
- Fagereng, Å., Den Hartog, S.A., 2017. Subduction megathrust creep governed by pressure solution and frictional-viscous flow. *Nat. Geosci.* 10 (1), 51–57.
- Fagereng, Å., Hillary, G.W., Diener, J.F., 2014. Brittle-viscous deformation, slow slip, and tremor. *Geophys. Res. Lett.* 41 (12), 4159–4167.
- Festa, A., Pini, G.A., Dilek, Y., Codegone, G., 2010. Mélanges and mélange-forming processes: a historical overview and new concepts. *Int. Geol. Rev.* 52 (10–12), 1040–1105.
- Frank, W.B., Shapiro, N.M., Husker, A.L., Kostoglodov, V., Bhat, H.S., Campillo, M., 2015. Along-fault pore-pressure evolution during a slow-slip event in Guerrero, Mexico. *Earth Planet. Sci. Lett.* 413, 135–143.
- French, M.E., Zhu, W., 2017. Slow fault propagation in serpentinite under conditions of high pore fluid pressure. *Earth Planet. Sci. Lett.* 473, 131–140.
- Gao, X., Wang, K., 2017. Rheological separation of the megathrust seismogenic zone and episodic tremor and slip. *Nature* 543 (7645), 416–419.
- Ghidaoui, M.S., Zhao, M., McInnis, D.A., Axworthy, D.H., 2005. A review of water hammer theory and practice. *Appl. Mech. Rev.* 58, 49–75. <https://doi.org/10.1115/1.1828050>.
- Ghosh, A., Vidale, J.E., Sweet, J.R., Creager, K.C., Wech, A.G., Houston, H., Brodsky, E.E., 2010. Rapid, continuous streaking of tremor in Cascadia. *Geochem. Geophys. Geosyst.* 11 (12).
- Gomberg, J., Wech, A., Creager, K., Obara, K., Agnew, D., 2016. Reconsidering earthquake scaling. *Geophys. Res. Lett.* 43. <https://doi.org/10.1002/2016GL069967>.
- Goswami, A., Barbot, S., 2018. Slow-slip events in semi-brittle serpentinite fault zones. *Sci. Rep.* 8 (1), 6181.
- Grove, M., Bebout, G.E., Jacobson, C.E., Barth, A.P., Kimbrough, D.L., King, R.L., Zou, H., Lovera, O.M., Mahoney, B.J., Gehrels, G.E., Draut, A.E., 2008. The Catalina Schist: evidence for middle cretaceous subduction erosion of southwestern North America. *Geol. Soc. Am. Spec. Pap.* 436, 335–361.
- Hall, K., Houston, H., Schmidt, D., 2018. Spatial Comparisons of Tremor and Slow Slip as a Constraint on Fault Strength in the Northern Cascadia Subduction Zone. *Geochem. Geophys. Geosyst.* 19 (8), 2706–2718.
- Hawthorne, J.C., Bartlow, N.M., 2018. Observing and modeling the spectrum of a slow slip event. *J. Geophys. Res. Solid Earth* 123, 4243–4265. <https://doi.org/10.1029/2017JB015124>.
- Hawthorne, J.C., Rubin, A.M., 2013. Laterally propagating slow slip events in a rate and state friction model with a velocity-weakening to velocity-strengthening transition. *J. Geophys. Res. Solid Earth* 118 (7), 3785–3808.
- Hawthorne, J.C., Bostock, M.G., Royer, A.A., Thomas, A.M., 2016. Variations in slow slip moment rate associated with rapid tremor reversals in Cascadia. *Geochem. Geophys. Geosyst.* 17 (12), 4899–4919.
- Hayman, N.W., Lavier, L.L., 2014. The geologic record of deep episodic tremor and slip. *Geology* 42 (3), 195–198.
- He, C., Wang, Z., Yao, W., 2007. Frictional sliding of gabbro gouge under hydrothermal conditions. *Tectonophysics* 445 (3–4), 353–362.
- He, C., Luo, L., Hao, Q.M., Zhou, Y., 2013. Velocity-weakening behavior of plagioclase and pyroxene gouges and stabilizing effect of small amounts of quartz under hydrothermal conditions. *J. Geophys. Res. Solid Earth* 118 (7), 3408–3430.
- Hirose, H., Obara, K., 2005. Repeating short-and long-term slow slip events with deep tremor activity around the Bungo channel region, Southwest Japan. *Earth Planets Space* 57 (10), 961–972.
- Houston, H., 2001. Influence of depth, focal mechanism, and tectonic setting on the shape and duration of earthquake source time functions. *J. Geophys. Res. Solid Earth* 106 (B6), 11137–11150.
- Houston, H., Delbridge, B.G., Wech, A.G., Creager, K.C., 2011. Rapid tremor reversals in Cascadia generated by a weakened plate interface. *Nat. Geosci.* 4 (6), 404.
- Hu, Y., Bürgmann, R., Uchida, N., Banerjee, P., Freymueller, J.T., 2016. Stress-driven relaxation of heterogeneous upper mantle and time-dependent afterslip following the 2011 Tohoku earthquake. *J. Geophys. Res. Solid Earth* 121 (1), 385–411.
- Ide, S., 2008. A Brownian walk model for slow earthquakes. *Geophys. Res. Lett.* 35 (17).
- Ide, S., 2010. Quantifying the time function of nonvolcanic tremor based on a stochastic model. *J. Geophys. Res. Solid Earth* 115 (B8).
- Ide, S., Maury, J., 2018. Seismic moment, seismic energy, and source duration of slow earthquakes: Application of Brownian slow earth-quake model to three major subduction zones. *Geophys. Res. Lett.* 45, 3059–3067. <https://doi.org/10.1002/2018GL077461>.
- Ide, S., Beroza, G.C., Shelly, D.R., Uchide, T., 2007. A scaling law for slow earthquakes.

- Nature 447 (7140), 76–79.
- Ide, S., Imanishi, K., Yoshida, Y., Beroza, G.C., Shelly, D.R., 2008. Bridging the gap between seismically and geodetically detected slow earthquakes. *Geophys. Res. Lett.* 35 (10).
- Ito, Y., Obara, K., 2006. Dynamic deformation of the accretionary prism excites very low frequency earthquakes. *Geophys. Res. Lett.* 33 (2).
- Ito, Y., Obara, K., Shiomi, K., Sekine, S., Hirose, H., 2007. Slow earthquakes coincident with episodic tremors and slow slip events. *Science* 315 (5811), 503–506.
- Kohlstedt, D.L., Evans, B., Mackwell, S.J., 1995. Strength of the lithosphere: constraints imposed by laboratory experiments. *J. Geophys. Res. Solid Earth* 100 (B9), 17587–17602.
- Li, S., Freymueller, J., McCaffrey, R., 2016. Slow slip events and time-dependent variations in locking beneath lower Cook Inlet of the Alaska-Aleutian subduction zone. *J. Geophys. Res. Solid Earth* 121 (2), 1060–1079.
- Liu, Y., 2014. Source scaling relations and along-strike segmentation of slow slip events in a 3-D subduction fault model. *J. Geophys. Res. Solid Earth* 119 (8), 6512–6533.
- Liu, Y., Rice, J.R., 2007. Spontaneous and triggered aseismic deformation transients in a subduction fault model. *J. Geophys. Res. Solid Earth* 112 (B9).
- Luo, Y., Ampuero, J.P., 2018. Stability of faults with heterogeneous friction properties and effective normal stress. *Tectonophysics* 733, 257–272.
- Madariaga, R., 1977. High-frequency radiation from crack (stress drop) models of earthquake faulting. *Geophys. J. R. Astron. Soc.* 51 (3), 625–651.
- Michel, S., Gualandi, A., Avouac, J.P., 2018. Interseismic coupling and slow slip events on the Cascadia megathrust. *Pure Appl. Geophys.* 1–25.
- Nielsen, S., Spagnuolo, E., Violay, M., Smith, S., Di Toro, G., Bistacchi, A., 2016. G: fracture energy, friction and dissipation in earthquakes. *J. Seismol.* 20 (4), 1187–1205.
- Obara, K., 2002. Nonvolcanic deep tremor associated with subduction in southwest Japan. *Science* 296 (5573), 1679–1681.
- Obara, K., Kato, A., 2016. Connecting slow earthquakes to huge earthquakes. *Science* 353 (6296), 253–257.
- Obara, K., Hirose, H., Yamamizu, F., Kasahara, K., 2004. Episodic slow slip events accompanied by non-volcanic tremors in Southwest Japan subduction zone. *Geophys. Res. Lett.* 31 (23).
- Ochi, T., Kato, T., 2013. Depth extent of the long-term slow slip event in the Tokai district, Central Japan: a new insight. *J. Geophys. Res. Solid Earth* 118 (9), 4847–4860.
- Ohnaka, M., Yamashita, T., 1989. A cohesive zone model for dynamic shear faulting based on experimentally inferred constitutive relation and strong motion source parameters. *J. Geophys. Res. Solid Earth* 94 (B4), 4089–4104.
- Pec, M., Stünitz, H., Heilbronner, R., Drury, M., 2016. Semi-brittle flow of granitoid fault rocks in experiments. *J. Geophys. Res. Solid Earth* 121 (3), 1677–1705.
- Peng, Z., Gomberg, J., 2010. An integrated perspective of the continuum between earthquakes and slow-slip phenomena. *Nat. Geosci.* 3 (9), 599.
- Peng, Y., Rubin, A.M., 2016. High-resolution images of tremor migrations beneath the Olympic Peninsula from stacked array of arrays seismic data. *Geochem. Geophys. Geosyst.* 17 (2), 587–601.
- Platt, J.P., Xia, H., Schmidt, W.L., 2018. Rheology and stress in subduction zones around the aseismic/seismic transition. *Prog. Earth Planet. Sci.* 5, 1–12.
- Radiguet, M., Cotton, F., Vergnolle, M., Campillo, M., Walpersdorf, A., Cotte, N., Kostoglodov, V., 2012. Slow slip events and strain accumulation in the Guerrero gap, Mexico. *J. Geophys. Res.* 117, B04305. <https://doi.org/10.1029/2011JB008801>.
- Radiguet, M., Perfettini, H., Cotte, N., Gualandi, A., Valette, B., Kostoglodov, V., Lhomme, T., Walpersdorf, A., Cano, E.C., Campillo, M., 2016. Triggering of the 2014 Mw7.3 Papanao earthquake by a slow slip event in Guerrero, Mexico. *Nat. Geosci.* 9 (11), 829–833.
- Rogers, K., Dragert, H., 2003. Episodic tremor and slip on the Cascadia subduction zone: the chatter of silent slip. *Science* 300 (5627), 1942–1943.
- Romanet, P., Bhat, H.S., Jolivet, R., Madariaga, R., 2018. Fast and slow slip events emerge due to fault geometrical complexity. *Geophys. Res. Lett.* 45 (10), 4809–4819.
- Rousset, B., Campillo, M., Lasserre, C., Frank, W.B., Cotte, N., Walpersdorf, A., Socquet, A., Kostoglodov, V., 2017. A geodetic matched filter search for slow slip with application to the Mexico subduction zone. *J. Geophys. Res. Solid Earth*. <https://doi.org/10.1002/2017JB014448>.
- Rubin, A.M., 2008. Episodic slow slip events and rate-and-state friction. *J. Geophys. Res. Solid Earth* 113 (B11).
- Rubin, A.M., 2011. Designer friction laws for bimodal slow slip propagation speed. *Geochem. Geophys. Geosyst.* 12 (4).
- Schwartz, S.Y., Rokosky, J.M., 2007. Slow slip events and seismic tremor at circum-Pacific subduction zones. *Rev. Geophys.* 45 (3) (8755-1209/07/2006RG000208).
- Segall, P., Rubin, A.M., Bradley, A.M., Rice, J.R., 2010. Dilatant strengthening as a mechanism for slow slip events. *J. Geophys. Res. Solid Earth* 115 (B12).
- Shapiro, N.M., Campillo, M., Kaminski, E., Vilotte, J.-P., Jaupart, C., 2018. Low-frequency earthquakes and pore pressure transients in subduction zones. *Geophys. Res. Lett.* 45, 11,083–11,094. <https://doi.org/10.1029/2018GL079893>.
- Shelly, D.R., Hardebeck, J.L., 2010. Precise tremor source locations and amplitude variations along the lower-crustal Central San Andreas Fault. *Geophys. Res. Lett.* 37 (14).
- Shelly, D.R., Beroza, G.C., Ide, S., 2007. Non-volcanic tremor and low-frequency earthquake swarms. *Nature* 446 (7133), 305.
- Shibazaki, B., Shimamoto, T., 2007. Modelling of short-interval silent slip events in deeper subduction interfaces considering the frictional properties at the unstable–stable transition regime. *Geophys. J. Int.* 171 (1), 191–205.
- Shibazaki, B., Obara, K., Matsuzawa, T., Hirose, H., 2012. Modeling of slow slip events along the deep subduction zone in the Kii Peninsula and Tokai regions, Southwest Japan. *J. Geophys. Res. Solid Earth* 117 (B6).
- Shimamoto, T., Noda, H., 2014. A friction to flow constitutive law and its application to a 2-D modeling of earthquakes. *J. Geophys. Res. Solid Earth* 119 (11), 8089–8106.
- Simons, M., Minson, S.E., Sladen, A., Ortega, F., Jiang, J., Owen, S.E., Meng, L., Ampuero, J.P., Wei, S., Chu, R., Helmberger, D.V., 2011. The 2011 magnitude 9.0 Tohoku-Oki earthquake: mosaicking the megathrust from seconds to centuries. *Science* 332 (6036), 1421–1425.
- Thurber, C.H., Zeng, X., Thomas, A.M., Audet, P., 2014. Phase-weighted stacking applied to low-frequency earthquakes. *Bull. Seismol. Soc. Am.* 104 (5), 2567–2572.
- Todd, E.K., Schwartz, S.Y., Mochizuki, K., Wallace, L.M., Sheehan, A.F., Webb, S.C., Williams, C.A., Nakai, J., Yarce, J., Fry, B., Henrys, S., 2018. Earthquakes and tremor linked to seamount subduction during shallow slow slip at the Hikurangi Margin, New Zealand. *J. Geophys. Res. Solid Earth* 123 (8), 6769–6783.
- Tong, X., Lavier, L.L., 2018. Simulation of slip transients and earthquakes in finite thickness shear zones with a plastic formulation. *Nat. Commun.* 9 (1), 3893.
- Violay, M., Gibert, B., Mainprice, D., Burg, J.P., 2015. Brittle versus ductile deformation as the main control of the deep fluid circulation in oceanic crust. *Geophys. Res. Lett.* 42, 2767–2773. <https://doi.org/10.1002/2015GL063437>.
- Violay, M., Heap, M.J., Acosta, M., Madonna, C., 2017. Porosity evolution at the brittle-ductile transition in the continental crust: implications for deep hydro-geothermal circulation. *Sci. Rep.* 7 (1), 7705.
- Wallace, L.M., Beavan, J., Bannister, S., Williams, C., 2012. Simultaneous long-term and short-term slow slip events at the Hikurangi subduction margin, New Zealand: implications for processes that control slow slip event occurrence, duration, and migration. *J. Geophys. Res. Solid Earth* 117 (B11).
- Wallace, L.M., Webb, S.C., Ito, Y., Mochizuki, K., Hino, R., Henrys, S., Schwartz, S.Y., Sheehan, A.F., 2016. Slow slip near the trench at the Hikurangi subduction zone, New Zealand. *Science* 352 (6286), 701–704.
- Wang, K., Bilek, S.L., 2014. Invited review paper: fault creep caused by subduction of rough seafloor relief. *Tectonophysics* 610, 1–24.
- Wang, K., Tréhu, A.M., 2016. Invited review paper: some outstanding issues in the study of great megathrust earthquakes—the Cascadia example. *J. Geodyn.* 98, 1–18.
- Yang, H., Liu, Y., Lin, J., 2012. Effects of subducted seamounts on megathrust earthquake nucleation and rupture propagation. *Geophys. Res. Lett.* 39 (24).
- Yang, H., Liu, Y., Lin, J., 2013. Geometrical effects of a subducted seamount on stopping megathrust ruptures. *Geophys. Res. Lett.* 40 (10), 2011–2016.
- Yin, A., 2018. Water hammers tremors during plate convergence. *Geology* 46 (12), 1031–1034.
- Yin, A., Xie, Z.M., Meng, L.S., 2018. A viscoplastic shear-zone model for deep (15–50 km) slow-slip events at plate convergent margins. *Earth Planet. Sci. Lett.* 491 (2018), 81–94.